

Article

A Recursive Wheel Wear and Vehicle Dynamic Performance Evolution Computational Model for Rail Vehicles with Tread Brakes

Smitirupa Pradhan  and Arun Kumar Samantaray *

Center for Railway Research (CRR-IIT Kharagpur), Department of Mechanical Engineering, Indian Institute of Technology (IIT), Kharagpur 721302, India; smitirupa@mech.iitkgp.ernet.in

* Correspondence: samantaray@mech.iitkgp.ac.in

Received: 22 March 2019; Accepted: 11 April 2019; Published: 17 April 2019



Abstract: The increased temperature of the rail wheels due to tread braking causes changes in the wheel material properties. This article considers the dynamic wheel material properties in a wheel wear evolution model by synergistically combining a multi-body dynamics vehicle model with a finite element heat transfer model. The brake power is estimated from the rail-wheel contact parameters obtained from vehicle model and used in a finite element model to estimate the average wheel temperature. The wheel temperature is then used for wheel wear computation and the worn wheel profile is fed to the vehicle model, thereby forming a recursive simulation chain. It is found that at a higher temperature, the softening of the rail-wheel material increases the rate of wheel wear. The most affected dynamic performance parameter of the vehicle is found to be the critical speed, which reduces sharply as the wheel wear exceeds a critical limit.

Keywords: tread braking; wheel-rail contact; tread wear; vehicle dynamics

1. Introduction

Several types of braking systems are used in railway vehicles. Tread braking along with electro-dynamic/disc braking is frequently used in freight, and low-speed suburban and metro trains due to its lower manufacturing cost, simple structure and ease of control. During tread braking, brake shoes/blocks press against the wheel tread and frictional heat is generated both at the wheel-brake block and wheel-rail interfaces. The heat generated due to braking is shared by the wheel, rail and block through thermal resistances and heat capacities [1]. Some amount of heat is also transferred into the surrounding through convection and radiation. Due to thermo-mechanical interaction, hot spots are often found on the wheel tread [2,3]. The amount of heat transfer between two contact-surfaces can be explained by the concept of third body approach [4], where wear debris, contaminants, sand, lubricant and leaves, etc. represent the third body.

There is a wide range of literature which contains both numerical approaches and experimental studies to understand the concept of heat transfer between the wheel-rail and wheel-block interfaces. The temperature rise due to slip at the wheel-rail interface has been studied by Tanvir [5]. Knothe and Liebelt [6] have studied the contact temperature at the wheel-rail contact surface due to sliding motion, where they have reduced a three-dimensional problem to a two-dimensional one, as an approximation. Furthermore, they have evaluated the effect of roughness and surface defect on the temperature distribution.

Ertz and Knothe [7] have calculated the temperature distribution on the wheel due to rolling along with sliding friction and concluded that the temperature rise due to braking is confined within a very thin layer near the contact surface. Among other notable works, Ma et al. [8] studied the tribological

responses on the surface and sub-surface of the wheel-rail interface for different operating conditions, Tudor et al. [9] developed an analytical solution for the temperature distribution at the wheel–rail and wheel–brake block contact surfaces, Spiriyagin et al. [10] studied the temperature distribution at the wheel flange–rail head interface, Naeimi et al. [11] computed flash temperature and stress-strain responses, Chen and Wang [12] analyzed the thermo-mechanical behavior of elasto-plastic bodies to study the impact of sliding speed and thermal softening on the contact behavior, and Kennedy et al. [13] built a finite element (FE) model to estimate the temperature distribution and heat partition between wheel and rail. Moreover, the effect of thermal loading on the fatigue life of the wheel is studied in [14,15], on material deformation and damage in [16] and on the bearing life in [17].

Many researchers have focused on the temperature distribution on the wheel profile due to constant brake power which is not comparable to the actual operating conditions. In this article, variable brake power similar to the real operating conditions is considered. The temperature at the tread of the wheel can rise up to 550 °C and in some extreme cases, it can go up to 800 °C [18]. Sometimes, the temperature may rise approximately up to 1050 °C due to skidding and locking of the wheels along the rail for a short span of time, as shown in the experimental results [19,20]. This causes phase transformations in the steel and leads to spall formation or wheel flat. Moreover, due to thermal loading, plastic deformation takes place and the microstructure on the wheel–tread surface changes. However, the aforementioned case is beyond the scope of the current research work. The accompanying thermal stresses and thermal softening due to elevated temperature increase the wheel wear rate. At higher temperature, the influence of thermal softening on wear rate is more pronounced than thermal stresses [21]. When the temperature due to braking is in the range of 300–350 °C, the wheel is more resistant to fatigue due to strain hardening [22].

Depending upon the operating conditions, single or multi point contact patches [23] occur at the tread and tread-flange. To calculate wear distribution, it is necessary to know the location of the contact patch, slip between the wheel and rail and the contact forces. Several researchers have suggested a number of approaches to predict the wear distribution in the wheels of the railway vehicles. The consequences of the worn wheel on the dynamics of the vehicle (such as creep force, creepage, critical and derailment speeds as well as change of size and location of the contact patches) are analyzed in limited literature, though its heavy wear is known to be detrimental to vehicle performance. Therefore, friction modifiers [24] are often used in tracks.

Although, the wheel and rail surfaces are rough due to wear, for simplifying the problem, it is assumed that the surfaces are smooth. Archard [25] has shown that the surface roughness has negligible effect on heat conduction. Several researchers focused on the estimation of the wear distribution due to braking [26,27]. In [26], disc brakes are used in the wheels and hence, the thermal influence on wheel/rail material properties is neglected. A very limited work has been reported on the wear distribution by considering the effect of wheel temperature during tread braking.

The objective of the present study is to estimate the wear distribution on the wheel profile by considering both thermal (from tread braking) and mechanical loadings (from wheel–rail contact forces) and the influence of worn wheels on the dynamic behavior of the vehicles at different depths of wear. The key contribution of this work is development of a thermo-mechanical wear model by combining multi-body dynamics and FE modeling in a recursive simulation framework. The wheel wear is shown to increase due to inclusion of thermo-mechanical material properties (change in material parameters of interest, such as density, hardness, Poisson's ratio and Kalker's creep coefficients) in the model of the tread-braked wheel. Consequently, another objective of this work is to determine the vehicle stability, derailment conditions and the passenger comfort as the wheel wear progresses with time. The motivation for such a study comes from the operational needs of railway operators to determine the ageing vehicle's safe speed limit in different sections of the track and to schedule its wheel re-profiling interval, accordingly.

2. Materials and Methods

The objective of this study is to develop a wear evolution model by considering the influence of temperature on the wheel material due to tread braking. The schematic representation of the recursive wheel wear and vehicle dynamics evolution process is shown in Figure 1. This tool deals with the estimation of wear distribution at the wheel surface under realistic vehicle operation by considering the change in material properties at the elevated temperature. During running, the vehicle accelerates, decelerates (including slowing before the curves and stop braking) and moves at constant velocity (intermediate cooling period). The temperature change in the brake block-wheel-rail system is estimated as per the vehicle operating condition. The model is composed of three interactive interfaces, namely the vehicle model, thermal model and wear model. The vehicle model is built in commercial multi-body simulation (MBS) software, VI-Rail™ in which dynamic simulation is performed. The outputs such as creepage (lateral, longitudinal and spin), instantaneous rolling radius, location of the contact patch, creep forces, etc. are collected from post-processing of the results from the dynamic simulation. Creep forces and creepages as per the specified vehicle speed profile are then used to calculate the brake power at the blocks and the contact patch on the rail. The thermal model is developed by using FE approach where heat fluxes corresponding to the brake power are generated at the brake blocks and the contact patch on the rail. The temperature field is found from this analysis and the corresponding changes in the physical properties of the wheel material at the tread surface are determined by mapping those to the available experimental data. The changes in material properties and the vehicle dynamics simulation results (creepages, contact patch location and dimension, etc.) are then used in a MATLAB® program for calculating the wear distribution on the wheel surface. The worn wheel profile is then generated and used recursively for further dynamic analysis.

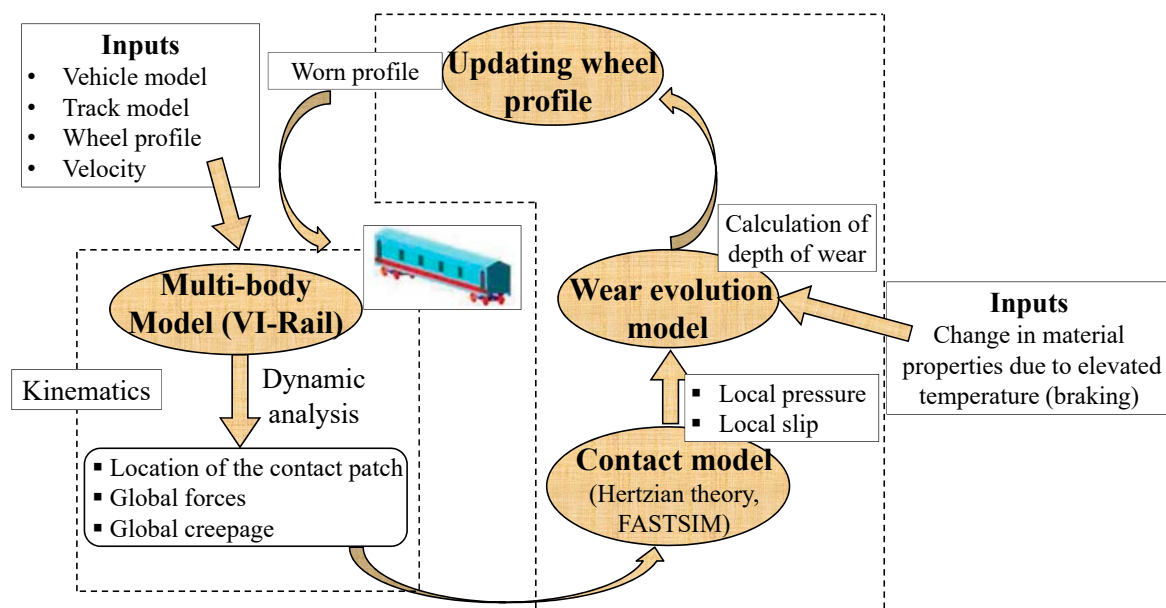


Figure 1. Architecture of recursive simulation model.

During the above-mentioned procedure, the main assumptions made to simplify the model are as follows:

- Wear in the rail is much less as compared to that in the wheel and hence is not taken into account.
- The contact between wheel and rail is in dry condition and the presence of a third body (worn particles of wheel, rail and block, water, sand and leaves) is not considered.
- The rail-wheel contact patch is elliptical in shape and the contact patch lies in the wheel tread, which is far away from the flange root.

- There is no wear in flange due to small duration, intermittent secondary contacts at entry and exit curves.
- The wheel and rail materials are same and have similar hardness.
- The wheel and rail material are isotropic, i.e., the material properties are same in all directions at a point but can vary from point to point due to change in temperature.
- The brake pad/shoe is made up of softer material (usually composite material with modulus of elasticity about ten times less as compared to wheel-rail material) and hence there is no wheel wear (but brake shoe/pad wear) at brake pad and wheel contact.
- The brake pads are assumed to be replaced periodically to maintain conformal contact between the brake pad and wheel tread, and the contact pressure between the wheel and brake pad is uniform.
- The heat partition between the wheel-rail-brake block is not influenced by the wheel wear.
- The influence of rail temperature variation is neglected in the model because it is usually much smaller than wheel temperature variation. Rail temperature is assumed to remain constant at 30 °C.
- Plastic deformation and fatigue effects are not considered.
- Spall formation, wheel flat etc. induced by phase transformation of the wheel and rail material at high contact pressure and temperature is neglected. The average contact patch pressure and temperature are considered for estimating the material properties while neglecting the local variations within the contact patch.

3. Wear Prediction Tool

3.1. Vehicle Model

An ERRI wagon/vehicle (Figure 2) with one coach and two bogies (front and rear) is used as a standard model for our research. The important components of the bogie are wheel (profile is s1002), secondary suspension system (air spring, secondary lateral and vertical dampers, anti-yaw damper and bump-stops) and the primary suspension system consists of axle box, helical spring and primary vertical damper as shown in Figure 2. The parametric values of the important components of the bogie are given in Table 1.

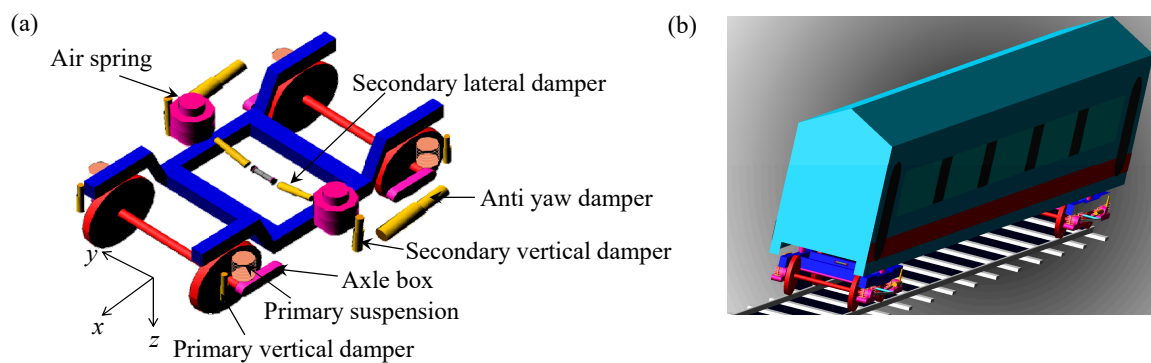


Figure 2. (a) Important bogie components and (b) Full vehicle model (two bogies with car body).

Table 1. Parameter values of important components of vehicle [26].

Parameters of MBS Model	Parameter Values	Quantity
Mass of car body	$M_{CB} = 32,000 \text{ kg}$	1
Rotary inertias of car body	$I_{xx} = 5.68 \times 10^4 \text{ kg m}^2$ $I_{yy} = 1.97 \times 10^6 \text{ kg m}^2$ $I_{zz} = 1.97 \times 10^6 \text{ kg m}^2$	
Mass of Bogie frame	$M_{bogie} = 2615 \text{ kg}$	2
Rotary inertias of bogie frame	$I_{xx} = 1722 \text{ kg m}^2$ $I_{yy} = 1476 \text{ kg m}^2$ $I_{zz} = 3067 \text{ kg m}^2$	
Mass of Wheel-set	$M_{wheel} = 1503 \text{ kg}$	4
Rotary inertias of wheel-set	$I_{xx} = 810 \text{ kg m}^2$ $I_{yy} = 810 \text{ kg m}^2$ $I_{zz} = 112 \text{ kg m}^2$	
Mass of Axle-box	$M_{abox} = 155 \text{ kg}$	8
Rotary inertias of axle box	$I_{xx} = 2.1 \text{ kg m}^2$ $I_{yy} = 5.6 \text{ kg m}^2$ $I_{zz} = 5.6 \text{ kg m}^2$	
Stiffness of Primary suspension	$K_x = 6.8 \times 10^6 \text{ N/m}$ $K_y = 3.92 \times 10^6 \text{ N/m}$ $K_z = 5.756 \times 10^5 \text{ N/m}$ $K_\theta = K_\alpha = 63.5 \text{ Nm/rad}$	8
Nominal pressure of Secondary suspension (Air spring)	$P_{static} = 2.0532 \times 10^5 \text{ Pa}$	4
Primary vertical damper (series stiffness)	$1.0 \times 10^6 \text{ N/m}$	8
Secondary vertical damper (series stiffness)	$6.0 \times 10^6 \text{ N/m}$	4
Secondary anti-yaw damper (series stiffness)	$3.0 \times 10^7 \text{ N/m}$	4
Secondary lateral damping (series stiffness)	$6.0 \times 10^6 \text{ N/m}$	4

In Table 1, K_x , K_y and K_z are the stiffnesses of the primary suspension in x , y and z directions, respectively, K_θ and K_α are the torsional stiffnesses in x and y directions, respectively. All the dampers are designed with nonlinear damping and series stiffness (standard data for ERRI bogie available in VI-RAIL). The standard ERRI bogie and coach parameters are considered (except primary suspension system) with air spring. To attain stability against hunting in a straight track, higher longitudinal and lateral stiffness of the primary suspension is required.

3.2. Track Model

Generally, flexible track is modeled separately in the VI-rail which is also the input parameter to the multi-body model for dynamic analysis. For the dynamic and thermal analysis, a flexible railway track between two Indian cities, Bhubaneswar and Cuttack of length 27.9 km has been considered (more details are given in [26]). This track comprises 69.4% straight, 14.9% transition and 15.65% curved portions as shown in Figure 3. The track design parameters are curvature, cant/super-elevation, transition curve, rail inclination, gauge and rail profile (UIC 60) and rail materials (Young modulus, Poisson's ratio), etc. The considered track consists of both small (smallest 526.3 m) and medium (largest 2000 m) curves. For estimation of critical speed and derailment speed, ramp type irregularities (width 5 mm and height 5 mm) are used.

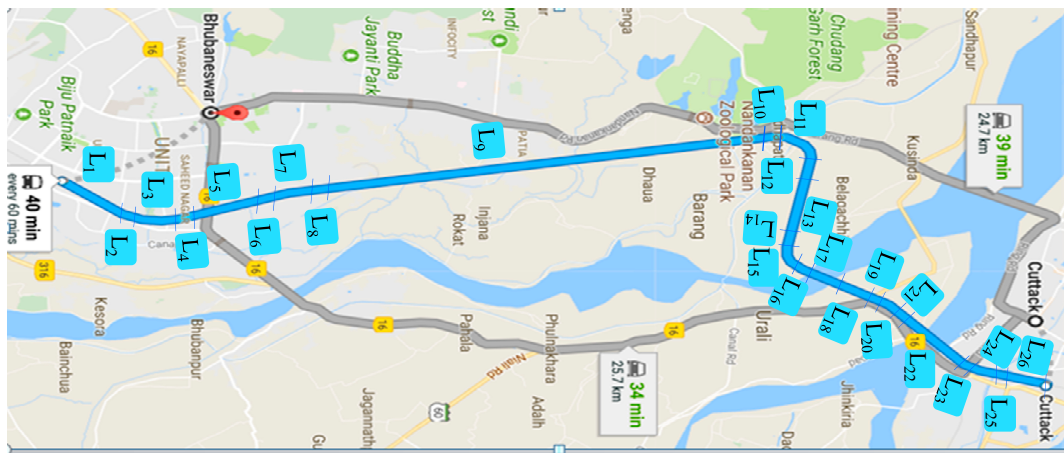


Figure 3. Track between two Indian cities Bhubaneswar and Cuttack at distance 27.9 km [26].

3.3. Thermal Model

Most of the railway vehicles in India employ mechanical braking such as tread braking and axle mounted disc braking. In tread braking, brake blocks/shoes directly come into contact with the tread of the wheel to stop and/or decelerate the vehicle. Depending on the application, different types such as clasp and tandem block arrangements (One/two block/s per wheel) are used. In this paper, two blocks per wheel and clasp arrangement (Figure 4a) is used for the analysis. Heat is generated due to friction at the brake shoe and moving tread interface and heat is transferred into the wheel and rail along with the brake shoe (as shown in Figure 4b). The part of heat transferred to the wheel (heat partition factor) depends on total contact area, total heat capacity of blocks and cooling conditions (as shown in Figure 4b), which is calculated as [28,29].

$$\beta = \left\{ 1 + \left(\frac{\kappa_w}{\kappa_b} \right)^{1/2} \frac{\lambda_b A_b}{\lambda_w A_w} \right\}^{-1} \tag{1}$$

Here, A is the area in contact, κ is thermal diffusivity, λ is thermal conductivity, subscripts b and w stand for brake block and wheel, respectively. The part of total heat transferred into the block is expressed as $(1 - \beta)$. After calculating the heat partition factor, the thermal analysis is straightforward with known brake power/heat fluxes at the contact surfaces.

The dimensionless Peclet number is $Pe = aV/2\kappa$, where a is semi-axis length of the contact patch in the rolling direction, V is the peripheral velocity of the wheel with thermal diffusivity $\kappa = \lambda/\rho C_p$ which depends on thermal conductivity, mass density (ρ) and specific heat capacity of the material (C_p). Pe helps to determine the type (1D/2D/3D) of heat conduction. In this paper, the minimum velocity is 16.8 m/s except stop braking, the size of a varies from 4.9 mm to 7.2 mm as the velocity varies with time. The thermal diffusivity for steel is $\kappa = 14.2 \times 10^{-6} \text{ m}^2/\text{s}$ [7]. The minimum estimated value of Pe is 5797 except during stop braking, which determines that the heat conduction occurs only normal to the contact plane, i.e., in z -direction as $Pe > 10$ [30]. Therefore, by neglecting longitudinal and lateral heat conduction (x and y direction), the one-dimensional heat conduction equation is given by

$$\kappa \frac{\partial^2 T}{\partial z^2} = \frac{\partial T}{\partial t} \tag{2}$$

where T stands for the instantaneous temperature and t is the time.

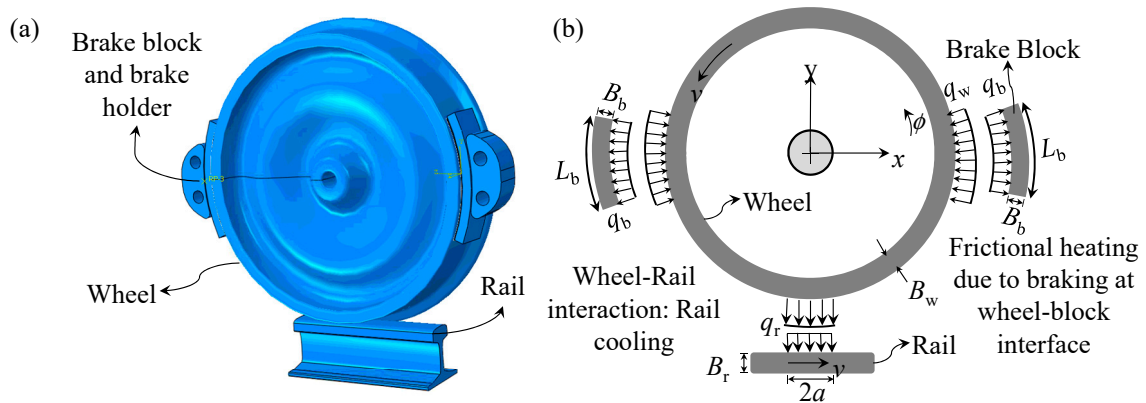


Figure 4. (a) Wheel-brake block-rail assembly and (b) Schematic diagram of distribution of frictional heat fluxes (q_w and q_b) at block-wheel interface and cooling flux (q_r) at wheel-rail interface.

The frictional power is generated during braking, which is converted into heat in the corresponding contact area (wheel–brake block and wheel–rail). To estimate the steady temperature, the commercial FE package, ABAQUS/Standard was used to model wheel–block–rail system (as shown in Figure 4a) which is a three-dimensional model. The block and block holder are modeled by FE approach as well. The mean heat flux over the brake block contact area is calculated as

$$q_{\text{brake}} = \frac{Q_{\text{brake}}}{H_b L_b} \tag{3}$$

where Q_{brake} is the thermal power generated during braking, block length (L_b) and block width (H_b) are 320 mm and 80 mm, respectively [31]. The amount of the brake power depends on the operating conditions of the vehicle. The vehicle reduces its velocity when it enters the transition and the curved portions of the track. Hence, the braking power varies according to the velocity profile as shown in Figure 5. The transient heat transfer can be explained by a conduction–convection (convection-diffusion) equation, i.e.,

$$\underbrace{\text{div}(\mathbf{K}\nabla T)}_{\text{Diffusion}} = C_p \rho \left(\frac{\partial T}{\partial t} + \underbrace{\mathbf{v} \cdot \nabla T}_{\text{Convection}} \right) \tag{4}$$

where div is the divergence vector operator, \mathbf{K} is the thermal conductivity matrix, ∇ refers to the vector differential operator and $\mathbf{v} = [v_x(x, y), v_y(x, y)]^T$ the velocity vector of spatial points [31]. During the curving, the braking force (F_b) (as shown in Figure 6, where R_x and R_y are reactions at axle in the x and y directions, respectively) acting on the wheel due to braking (deceleration) and corresponding braking power is calculated.

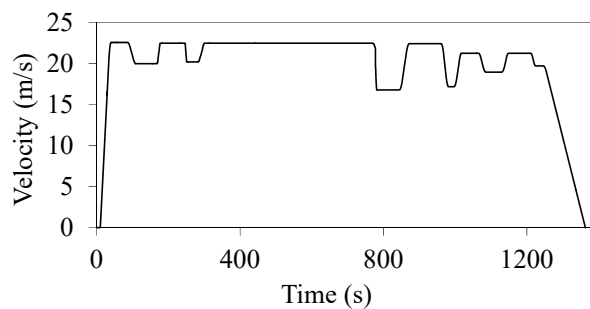


Figure 5. Velocity profile for acceleration and braking.

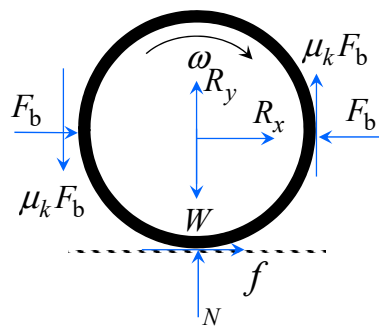


Figure 6. Calculation of brake force in curved track.

It is assumed that the power generated due to friction is dissipated as heat over the common contact area between block and wheel and total heat generated is partitioned between the wheel and block. By neglecting longitudinal rail gradient, buff and draft forces, etc. the power at the wheel-block interface during braking is estimated by solving

$$J\ddot{\theta} = -(2\mu_k F_b - f)R, \tag{5}$$

$$P_{\text{brake}} = 2\mu_k F_b \omega R \text{ for } \ddot{\theta} < 0 \tag{6}$$

where J is the polar moment of inertia of wheel and axle, R the mean radius of the wheel at nominal tread region, μ_k ($\mu_k = 0.2$) the coefficient of kinematic friction (full slip) brake block-wheel interface, f the traction force at contact patch, F_b is the braking force generated during braking at blocks and $\omega = \dot{\theta}$ is the angular velocity of the wheel. Rail vehicles take a long time to stop and hence the slip at the rail-wheel interface is much smaller with respect to that at brake block-wheel interface.

In this research, the true traction force values obtained from dynamic simulation are utilized for brake force and power computation. Furthermore, for steady running on the smooth track with small suspension play, negligible lateral slip (brakes applied on straight portion of the track) and no rail-wheel contact separation, $f = \mu N$ and the instantaneous braking power generated at the wheel-rail interface is given as

$$P_{\text{contact}} \cong \mu N(V - \omega R)\text{sign}(V - \omega R), \tag{7}$$

where $N, V, \omega, \dot{\omega}$ etc. are computed from the dynamic simulation in VI-Rail.

Note that brake blocks are not modeled in VI-Rail, only the velocity profile is provided, and brake forces are estimated externally through Equations (5) and (6). The velocity profile is input to the dynamic simulation and the time response of traction force f , normal reaction N , angular velocity $\omega = \dot{\theta}$ and angular acceleration $\ddot{\theta}$ are taken as outputs. These outputs are used in Equation (5) to compute brake force F_b and then to compute the frictional power generated at the brake block-wheel and rail-wheel interfaces. The frictional power, in the form of heat power, is then partitioned as shown in Figure 4b and used in the development of FE model to predict the wheel temperature evolution. Such coupled thermo-mechanical models have been used in the past for predicting the tire cornering characteristic variations in on-road vehicles [32]. The computation of heat generation at the contact patch does not consider the local effects such as stick-slip regions and traction limits; however, the averaged solution gives a fairly accurate estimate. Moreover, during braking, there is a load transfer from the rear to the front wheels. This load transfer is automatically accounted for by VI-Rail software. However, the load transfer is too small in comparison to the axle load and can be neglected.

The coefficient of friction (μ) is dependent on slip (creepage) velocity between wheel and rail, which was observed by several researchers and described in [26,33]. The slip dependent coefficient of friction can be expressed as

$$\mu = \mu_0 \left[(1 - A_0)e^{-B_0 s} + A_0 \right] \tag{8}$$

where A_0 stands for the ratio of friction coefficient (μ_∞/μ_0), B_0 is the coefficient of exponential friction decrease (in s/m) and s is the total slip or slip velocity (in m/s). For a dry wheel–rail contact scenario, $\mu_0 = 0.55$, $A_0 = 0.4$ and $B_0 = 0.6$ [34]. The variation of the coefficient of friction is shown in Figure 7 and is used to calculate brake power. The brake power on the wheel-block (P_{brake}) and the wheel–rail (P_{contact}) interfaces are calculated in Equations (6) and (7) and shown in Figure 8. The power generated at the wheel-rail contact due to friction is low as compared to brake power because there is full slip at the brake blocks.

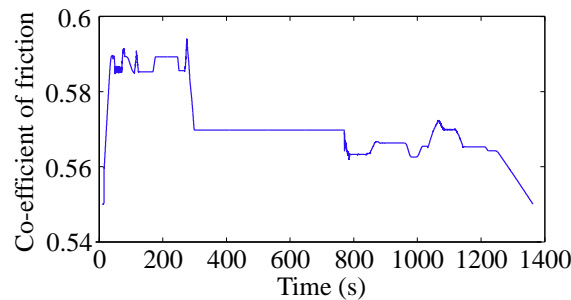


Figure 7. Variation of slip-dependent coefficient of friction along the simulated track.

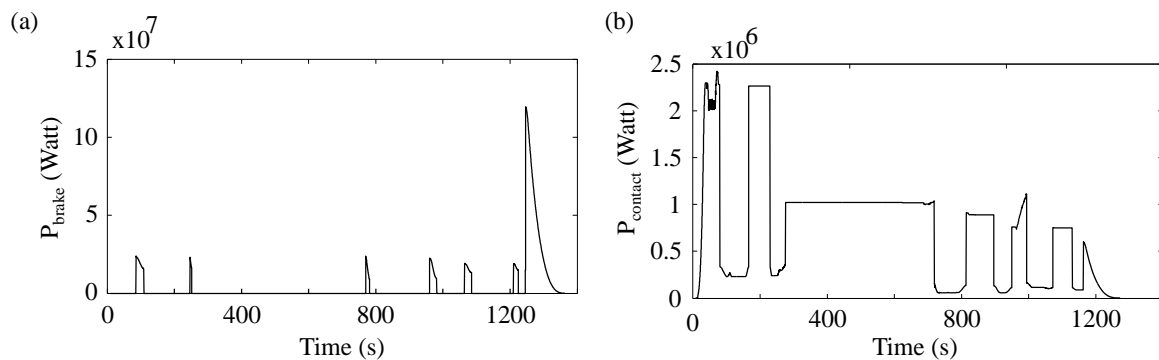


Figure 8. Estimated brake/traction power (P_{brake}) (a) at wheel-block and (b) wheel-rail interfaces.

The variation of heat flux on the circumference of the rotating wheel is taken into account while estimating the temperature rise at the tread surface. The generated brake power at the wheel–block interface increases the wheel tread temperature while the wheel and block are in contact and decreases after leaving the braking surface due to convection till the next block is in contact. Again, the temperature of brake block will decrease while the wheel comes in contact with rail due to the rail chill effect.

As the material of wheel and rail is the same, the temperature rise in the rail is the same as the temperature drop in case of wheel at a particular instant. Figure 9a shows ABAQUS FE mesh for block-wheel and wheel-rail contacts. This model is developed for the passenger vehicle. Hexagonal and tetrahedral elements are used for meshing the wheel and rail and block, respectively. The wheel, block, brake block holder and rail meshed with 27648, 9641, 6751 and 3918 elements. In this model, heat fluxes q_b and q_r are given to the blocks and rail, respectively, to estimate temperature field due to braking and contact at the rail. The finite thermal conductance h_{wr} (inverse of thermal contact resistance) at the rail-wheel interface is constant whose value is $h_{wr} = 3 \times 10^6 \text{ W/m}^2 \cdot \text{°C}$ [31]. It is assumed that heat flux is same for both the blocks (left and right of the wheel) for simplifying the problem. The heat transfer between wheel and rail surface is modeled as $q_w = q_r = h_{wr}(T_w - T_r)$, where $q_w (= q_r)$ are heat flux per unit area, suffices w and r are used for wheel and rail, respectively. The temperature of the rail is assumed to be equal to the ambient temperature ($T_r = 30 \text{ °C}$). Since, the contact between wheel and rail and wheel and brake block occurs for a very small span of time, the

thermal penetration depth ($\Delta = a / \sqrt{Pe}$) is 6.43×10^{-5} m (Figure 9b) which is small as compared to the size of the contact patch.

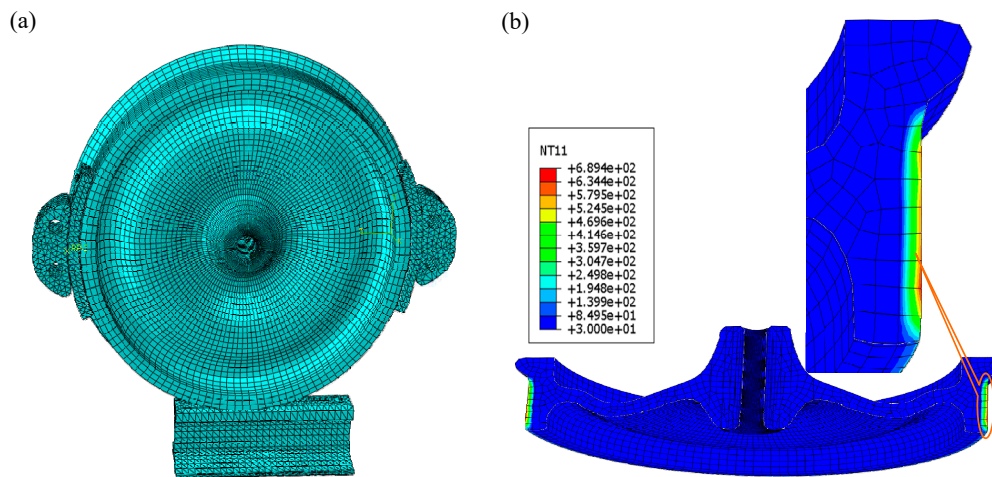


Figure 9. (a) Standard 3D FE model of wheel, braking system and rail assembly with meshing and (b) Temperature distribution on the surface of the wheel.

The influence of the cooling effect of the rail is also implemented here by using convection–diffusion boundary condition. The wheel–block–rail FE model is used to study the heat partitioning between block–wheel and rail–wheel for the above-mentioned brake powers (see Figure 8). The lateral position of the wheel with respect to rail is changed due to the presence of both straight (almost constant position as no irregularities are considered) and curved tracks. Due to frequent use of braking for decelerating the vehicle (different rate) and stop braking, the tread portion of the wheel attains the elevated temperatures. Additionally, heat loss due to convection is also included in this FE model. Heat flows from outside of the contact patch of the wheel to the surrounding by convection. The amount of heat transfer through the convection is given by $q_{\text{conv}} = -\alpha(T - T_{\infty})$; negative sign indicates that heat is leaving from the surface. In case of wheel, forced convection is due to rotation of wheel. The convective heat transfer in TGV railway wheel was measured by Dufrenoy [35] and an empirical relation $\alpha \approx 3.6 V$ was proposed to calculate the heat transfer coefficient (α) for the polished wheel tread and flange surfaces. Fischer et al. [36] used that empirical relation to analytically model the wheel temperature profile to frictional heat at the rail–wheel interface. The value of α varies with time as velocity varies. To simplify the problem, the maximum value of α is taken as 81 W/Km^2 ($V_{\text{max}} = 22.5 \text{ m/s}$ from Figure 5). Although the vehicle nose is designed to direct most of the air flow along the top and sides of the body, there is some air flow through the undercarriage clearance. Thus, the higher heat transfer coefficient partially accounts for the missing undercarriage flow velocity. Biot number ($Bi = \alpha l / \lambda_w$, $l = 2a$, λ_w is the thermal conductivity of wheel) is used to estimate the temperature gradient inside the solid. In this paper, $l = 2a = 9.8 \text{ mm}$ (from the dynamic simulation in VI-Rail software), $\lambda_w = 50 \text{ W/Km}$ [7], $Bi = 0.01323$. The temperature gradient inside solid can be neglected during estimating the convective heat transfer coefficient as $Bi < 0.1$ [37]. The boundary conditions of the FE model were updated after each time step of FE simulation because the rail–wheel contact patch and the portion of the wheel in contact with the brake changes with wheel rotation. The heat flux calculated from Equations (6) and (7) is averaged over the contact surface and partitioned between the mating surfaces. Those are then given as constant heat flux (for the time step) boundary condition at the mating surfaces. All the remaining boundary nodes of the wheel are given convective boundary condition. Note that as the wheel rotates, some elements leave the contact zone and some elements enter into it. Also, the heat flux changes with wheel speed variation, e.g., braking. Thus, the boundary conditions continually change.

3.4. Material Properties

Generally, thermo-mechanical properties of the steel are influenced by temperature variations. In the present research, the temperature dependent mechanical properties of wheel, rail and brake block act as input parameters to the wear model. The wheel and rail are made from steel (pearlite) with composition 0.5 C, 0.7 Mn, 0.3 Si, 0.15 Cr, 0.06 Mo, 0.1 Ni by percentage weight. The brake blocks and brake holders are made of composite material and cast iron, respectively. The physical properties of all the above-mentioned materials are given in Table 2. By using all the material properties (Table 2) the temperature distribution has been estimated for the total time period (1353 s), which is shown in Figure 10.

Table 2. Thermal properties for the wheel and rail, brake blocks and brake holder: Specific heat (C_p), thermal conductivity (λ), mass density (ρ) [2,31].

Material	C_p (J/kg °C)	λ (W/m °C)	ρ (kg/m ³)	E (GPa)	ν
Steel (wheel and rail)	460	51.9	7850	210	0.283
Composite (block)	1500	5	2670	10	0.25
Cast iron	520	48	7920	103	0.25

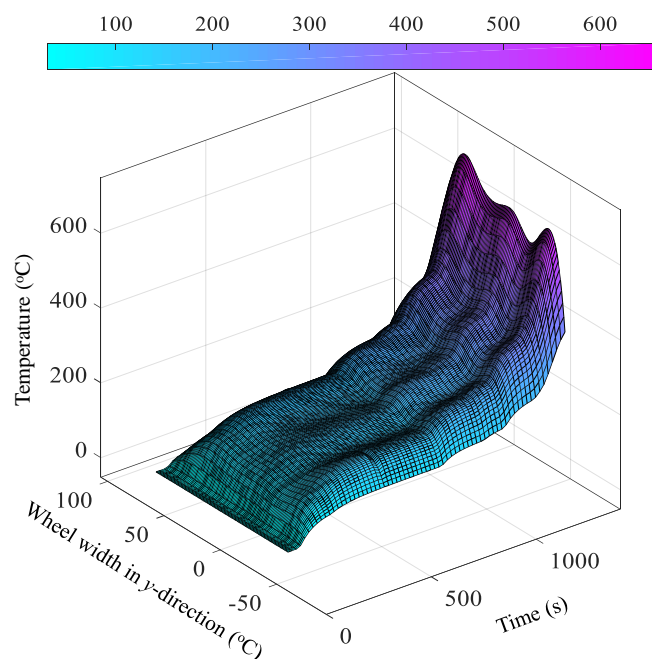


Figure 10. Temperature distribution on the wheel surface due to tread braking.

This temperature profile was obtained for the velocity profile (Figure 5) and track (Figure 3) when the vehicle traverses the entire length of the track. The total track of length 27.9 km is covered in 1363 s. Within this period, there is acceleration as well as braking, both of which generate longitudinal creepage and heat flux at the wheel-rail contact patch. Additional heat flux is generated at brake blocks during tread braking. Furthermore, there is lateral creepage during curves and lateral oscillations. After approximately 700 s (See Figure 5), there are frequent brakes and accelerations due to frequent curves in sections L₁₅ to L₂₆ of the track (see Figure 3). Therefore, the rate of heat generation increases during that period and the wheel temperature is highest when the vehicle is finally stop-braked to reach the terminal. The waviness seen in Figure 10 along the time axis corresponds to the temperature increase and cooling down effects due to acceleration, braking and steady run periods; whereas that along the y -direction is due to lateral shift in contact patch.

4. Wear Evolution Tool

4.1. Contact Model

The global contact parameters such as contact forces (longitudinal, lateral and normal), creepage (longitudinal, lateral and spin), rolling radius, contact angle, location of the contact patches and dimensions of the contact patches are collected at each integration step of post-processing of multi-body dynamic simulation in VI-Rail. The local contact parameters such as tangential (lateral and longitudinal) and normal contact pressure and local slip are evaluated within the contact patch from global contact parameters. The normal contact pressure is calculated by the Hertzian contact approach, whereas the tangential pressure and slip are estimated by Kalker’s FASTSIM approach [38], by assuming that the shape of the contact patch is elliptical irrespective of the location of the contact patch. Each contact patch is discretized into cells with $\Delta y = 2b/(n_y - 1)$ and $\Delta x(y) = 2a(y)/(n_x - 1)$, where n_x and n_y are the numbers of cells in x and y directions, respectively as shown in Figure 11.

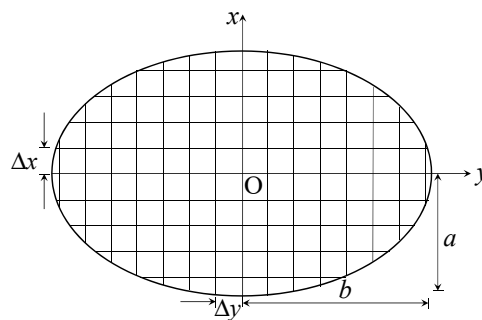


Figure 11. Discretization of elliptical contact patch.

The slip (s) is the combination of rigid slip and the derivative of the relative/elastic displacement between the particles of wheel and rail ($\mathbf{u} = \mathbf{u}^w - \mathbf{u}^r$). The slip at any cell (x, y) is calculated as [38]

$$\mathbf{s}(x, y) = \left[(v_x - \phi y), (v_y + \phi x) \right]^T + \dot{\mathbf{u}}(x, y, t) \tag{9}$$

where v_x, v_y and ϕ represent longitudinal, lateral and spin creepages [38,39], respectively.

In steady-state contact problem, $\partial \mathbf{u}(x, y) / \partial t = 0$

$$\mathbf{s}(x, y) \frac{\Delta x(y)}{V} = \mathbf{u}(x, y) - \mathbf{u}(x - \Delta x(y), y) + \left[(v_x - \phi y), (v_y + \phi x) \right]^T \Delta x(y) \tag{10}$$

and the elastic displacement in any grid/mesh within the contact patch is given by

$$\mathbf{u}(x, y) = L \mathbf{P}_t(x, y), L = L(\xi, a, b, G, \nu) \tag{11}$$

where L is flexibility function, \mathbf{P}_t is the tangential pressure, ξ is a global creepage vector, G is shear modulus and ν is the Poisson’s ratio. The flexibility factor/elasticity coefficient is expressed as $L = \frac{|\xi_x|L_1 + |\xi_y|L_2 + c|\xi_{sp}|L_3}{\sqrt{(\xi_x^2 + \xi_y^2 + c^2 \xi_{sp}^2)}}$, with $L_1 = 8a/(3Gc_{11}), L_2 = 8a/(3Gc_{22}), L_3 = \pi a \sqrt{a/b}/(4c_{23}G)$ and $c = \sqrt{ab}$ [38,40].

Kalker’s parameter, c_{ij} , is a function of a, b and ν . However, the shear modulus depends on the temperature. The physical properties of the rail and wheel material (both are same) are given in Figure 12. These properties are obtained from several experimentally validated physics-based materials modeling, which are implemented in JMatPro® software [41]. During the experiment to determine the material parameters, the samples are subjected to the average contact patch pressure which is computed from the contact patch size and the mean axle load. It can be seen that there is significant change in material properties with the temperature. The shear modulus of the material at the contact

patch is computed from the elastic modulus and Poisson’s ratio values for the wheel temperature at the given time and location on the track (Figure 10). In Figure 12, the effect of phase transformation is visible as a sudden change in the trend of variation of material with temperature in the temperature range between 600 °C and 800 °C. Thus, the phase transformation effect is implicitly included in the wear evolution model.

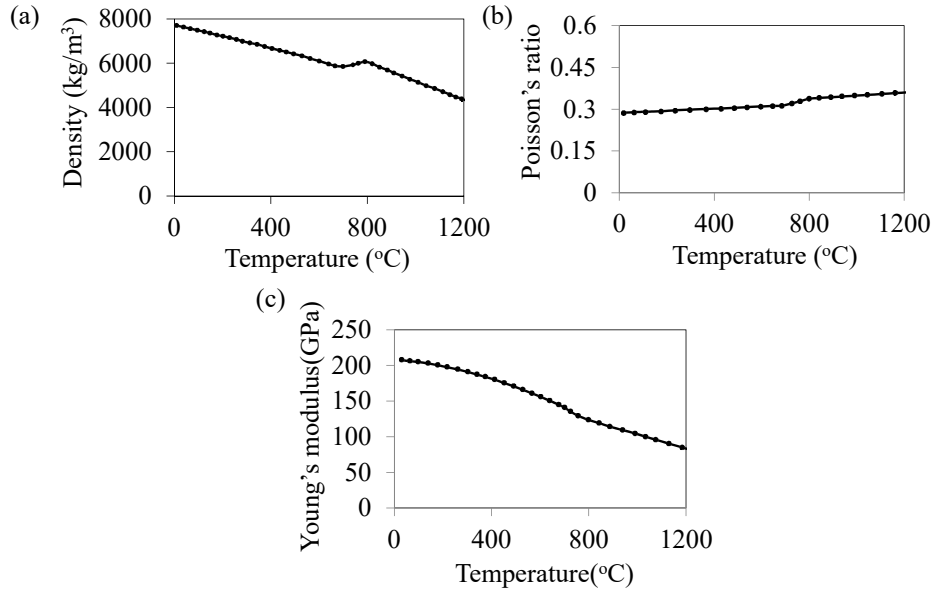


Figure 12. Change in physical properties of the material with temperature: (a) Density, (b) Poisson’s ratio and (c) Young’s modulus or modulus of elasticity.

The normal contact pressure for each cell within the elliptical contact patch is estimated in Equation (12) by using Hertz theory. The normal pressure distribution (P_n) [39] at any generic point (x, y), with $1 \leq x \leq n_x$ and $1 \leq y \leq n_y$ is given by

$$P_n(x, y) = P_0 \sqrt{1 - \frac{x^2}{a^2} - \frac{y^2}{b^2}} \tag{12}$$

where P_0 is the maximum pressure at (0,0). $P_0 = (3N/2\pi ab)$, where N stands for normal contact force.

If the considered cell inside the contact patch is within the adhesion region (where \mathbf{P}_A is the adhesion limit pressure) then

$$\begin{aligned} \|\mathbf{P}_A(x, y)\| &\leq \mu P_n(x, y) \Rightarrow \mathbf{P}_t(x, y) = \mathbf{P}_A(x, y), \\ \mathbf{P}_A(x, y) &= \mathbf{P}_t(x - \Delta x(y), y) - [(v_x - \phi y), (v_y + \phi y)]^T \Delta x(y), \mathbf{s}(x, y) = 0 \end{aligned} \tag{13}$$

Otherwise, slip occurs and

$$\|\mathbf{P}_A(x, y)\| > \mu P_n(x, y) \Rightarrow \begin{cases} \mathbf{P}_t(x, y) = \mu P_n(x, y) \mathbf{P}_A(x, y) / \|\mathbf{P}_A(x, y)\|, \\ \mathbf{s}(x, y) = \frac{LV}{\Delta x(y)} (\mathbf{P}_t(x, y) - \mathbf{P}_A(x, y)) \end{cases} \tag{14}$$

Equation (13) is applied for all the cells in the discretized contact patch. This is the same consideration used in [27,40]. As creepage and normal pressure distribution are zero outside of the contact patch, $\mathbf{P}_t(x, y) = 0$ and $\mathbf{s}(x, y) = 0$ there. Note that in this article, the material parameters are evaluated at the average contact patch pressure and temperature. The value P_0 occurs at the center of the contact patch and the pressure in its neighborhood is higher than the average pressure. Hence, ideally, the phase transformation should take place at a lower temperature in those cells; whereas the phase transformation for cells at lower pressure than average pressure, i.e., at the edge of the contact

patch, should take place at a higher temperature. However, to simplify the model and computation, such local effects for material parameter variation are not considered in the model developed in this article.

4.2. Wear Model

The wear distribution of the wheel profile is based on the volume of the material removed from the wheel surface, which is related to the total frictional work. Furthermore, due to tread braking, additional heat is generated at the block and the wheel and rail and wheel surfaces due to friction, which is observed in Figure 10.

The wear model developed by University of Sheffield (USFD) [42] is used here to estimate wear distribution. This model relates the wear rate, i.e., the weight of the lost material per distance rolled per contact area, to the wear index. Empirical wear constants for three wear regimes, which depend on the contacting materials as well as the frictional power, are introduced. The wear regimes are identified as mild, severe and catastrophic. Tread wear is considered to be in the mild regime whereas flange wear belongs to severe or catastrophic regime. Specific volume (volume per unit area per unit distance travelled (expressed as mm³/mm²m)) is the measure of amount of removal of material at any grid point (x, y), which is a function of time. Wear index (I_w in N/mm²) can be estimated by using the local frictional power developed by tangential contact pressure [40]:

$$I_w = \frac{P_t \cdot s}{V} \tag{15}$$

which is based on twin disk experimental data (Figure 13). The data were collected from the experimental test conducted on the roller rig for steel–steel (R8T wheel material and UIC 60 900A rail material) contact bodies under dry condition, presented in [40,43,44]. The wear test results on the twin-disk setup usually have a large spread. Therefore, statistically averaged trends are used to generate the wear map, i.e., the relation between the wear rate and the wear index. The fitted expression for wear rate $K(I_w)$ (in $\mu\text{g}/\text{m mm}^2$) is given as

$$K(I_w) = \begin{cases} 5.3I_w, & I_w < 10.4 \text{ N/mm}^2 \\ 55 & 10.4 \leq I_w \leq 77.2 \text{ N/mm}^2 \\ 61.9I_w - 4723 & I_w > 77.2 \text{ N/mm}^2 \end{cases} \tag{16}$$

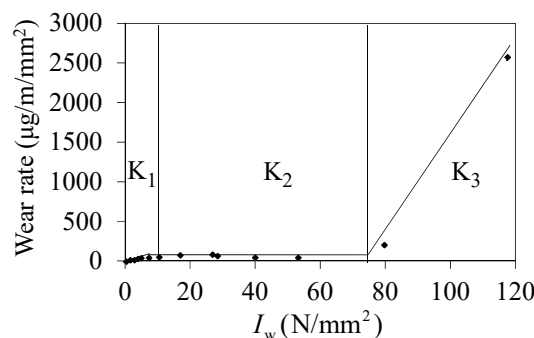


Figure 13. Wear map showing the wear rate as a function of wear index [40,43,44].

Note that the wheel temperature changes the shear modulus G (a function of Young’s modulus and Poisson’s ratio), which in turn changes the flexibility factor L and the elastic displacement \mathbf{u} defined in Equation (11). Therefore, the total slip s defined in Equation (10) becomes dependent on temperature. The local friction power I_w , as defined in Equation (14), depends on the slip s ; hence it is influenced by the temperature.

Generally, the wear rate is different from tread to flange; the wear rate on the tread and flange occur at the regimes K_1 , and K_1 and K_2 , respectively. The specific volume of the worn material from the wheel can be calculated after evaluating the wear rate as

$$\delta_p(x, y) = \frac{K(I_w)}{\rho} \quad (17)$$

The above estimated wear rate (Equation (16)) may be slightly different from the actual wear rate as plastic deformation and fatigue effects are not considered here. Note that the density of the material on the wheel tread changes due temperature (See Figure 12a) and hence the wear rate is doubly influenced by the wheel tread temperatures: first through the dependence of frictional power I_w on the shear modulus (function of Young's modulus, Poisson's ratio and temperature as shown in Figure 12b,c) and, second due to the density ρ (in Equation (16)) which also depends on the temperature (Figure 12a). As the temperature increases, there is appreciable reduction in Young's modulus and a small increase in Poisson's ratio, which implies that the shear modulus decreases appreciably with increase in temperature. Thus, at increased temperature, the flexibility factors and the frictional power increase. The frictional power determines the regime of wear, and the wear rate $K(I_w)$ (Equation (15)). Further, temperature reduces density. Thus, at higher temperature, the numerator in Equation (16) increases and the denominator decreases. As the material softens due to temperature, more frictional power is generated and the wear rate increases. That is how temperature effects are coupled to the wear rate.

The rail–wheel interaction is severely affected by the presence of a third body between their contact, such as wear debris, leaves, wood particles and sand. Usually, soft particulate matter on the rail is instantaneously crushed when the heavily loaded wheel comes over it. Weather conditions such as heat and humidity contributes to rail oxidation and corrosion, and this is especially severe in the coastal areas of India. Oxide formation significantly reduces adhesion/friction under wet condition [45] and similarly, crushed leaf layers reduce friction between the rail and the wheel [45,46]. On one hand, such reduced friction increases the chance of derailment and braking distance while on the other hand, reduced friction reduces the creep forces and hence the wheel and rail wear. However, rail corrosion is a much slower process and barely influences wheel wear. In coastal India, rail foot corrodes at a faster rate than the wear at rail top. Therefore, in coastal areas, rails are removed at half the life of those in the inland tracks. If the life of the rail is much larger than that of the wheels, then rail wear can be neglected during wheel wear modeling.

Note that the presence of hard particulate matter in the contact patch increases the rail and wheel wear through various modes such as abrasion, indentation and scuffing [47]. In the real track scenario considered here, there can be some variation in the friction coefficient over the length of the track due to various reasons. Also, seasonal effects (rain, wind, heat, leave fall at onset of dry season, etc.) influence the friction coefficient and these effects are too variable to be considered in the model. The wheel wear simulation conducted here considers duration of more than a year of wheel life (for at least 10 trips per day). Therefore, seasonal effects which sometimes increase and sometimes decrease the friction coefficient are assumed to average out and are neglected in the model.

There can be several high frequency or random irregularities, such as dents, undulations, scuffs, scratches, etc. present in the track. At a macroscopic level, the friction coefficient does not depend on small pits or dents on the track because the contact patch area at the rail-wheel contact is sufficiently large (approximately the size of a dime in circulation in the USA). It has been shown in previous research [26] that the creep forces calculated by neglecting high frequency track irregularities are almost the average of the creep forces calculated by considering the track irregularities, as long as the friction coefficient remains the same. The rail wear rate does not change appreciably due to consideration of these track irregularities. With large pits and dents, the wheel and rail wear rate increases. However, these tribological aspects are outside the scope of this article.

4.3. Procedure for Updating Wheel Profile

The wheel profile is updated through a series of numerical procedures starting from a new wheel profile s1002. The updating procedure is important as the adopted procedure may significantly affect the results. Although all the wheel-sets (combination of left and right wheels) of the railway vehicle have different wear rate, the wear distribution in only one set of wheels (front axle of front bogie) is presented in this paper. Since the wheel wears faster than rail, the wear of the wheel is considered only.

A set of numerical procedures provide a worn wheel profile from the new wheel profile [40,44]. The wear in longitudinal direction is computed as

$$\delta^{\text{tot}}(y) = \frac{1}{2\pi R(y)} \int_{-a(y)}^{a(y)} \delta_p(x, y) dx \quad (18)$$

where $a(y)$ is half of the length of a strip containing all the cells in the corresponding row of the discretized cell matrix in the contact ellipse (See Figure 11). The above expression (Equation (17)) integrates all the wear distribution at each grid (x, y) along the longitudinal or x -direction within the contact patch and extends/averages the wear along the circumference with rolling radius $R(y)$. Due to lateral shift of contact patch over the wheel profile, the contact patch locations need to be specified in a common reference frame. A parameterized curvilinear wheel reference frame [40,44] is thus used and a time integration of Equation (17) mapped to the wheel frame is then performed for the total duration of travel. Thereafter, the wear over all the contact patches are summed and further averaged. All these procedures such as estimation of total wear distribution, scaling, smoothening and updating the wheel profile is the same as in [26,41] and are thus, not repeated here. Note that the vehicle dynamics is a fast process whereas the wear evolution is a slow process. This basic premise is aptly described in [48]. Thus, the fast vehicle dynamics response as well as the temperature distribution is assumed to remain fixed between two-wheel wear update steps. After every wheel profile update, the vehicle dynamics for the whole track length with worn wheels and the specified velocity profile is re-simulated to generate the contact stresses, creepages and other parameters needed to compute the frictional power. The new data are used in FE simulation to generate the temperature profiles (as in Figure 10) with worn wheels. The new temperature profile is used to compute the material properties until the next wheel profile update step.

5. Results

A non-articulated train-set is considered here to study the dynamic behavior of the railway vehicle due to tread braking. Due to the train-set configuration (non-articulated) and no draft and buff forces, it is assumed that the dynamic behavior of each vehicle (one coach and two bogies) has no significant influence on other vehicles. Hence, each vehicle (see Section 3.1) can be studied independently. The track in between two cities of Bhubaneswar and Cuttack (Indian Railway track), is considered here to study the wear distribution. The length of the track is 27.9 km and the vehicle takes 1353 s to cover this distance with different velocities (as shown in Figure 5). For the study of the dynamic behavior as well as wear analysis, no track irregularities are considered, however, flexibility properties of the track have been taken into consideration. For the dynamic simulation, the main parameters are UIC 60 rail profile with rail inclination 1:40, s1002 wheel profile with diameter 920 mm, standard gauge (1435 mm) track. The wear distribution is estimated by performing several to and fro journeys on the designed track (see Figure 3), until covering the distance of 10,044 km. It is observed from the simulations that the wear rate is higher in the initial stages due to non-conformal contact between wheel and rail profiles and in the later stages, wear rate slows down due to more conformal contact. The estimated wear depths on the new wheel profile by considering the tread and disc braking are compared in Figure 14. Note that due to load transfer during braking, the normal reaction at wheel-rail contact is more in the front axle of the front bogie. Thus, the results pertaining to wheel wear are given for wheels in front axle of front

bogie. The new wheel profile and worn wheel profiles after covering 100,440 km distance with tread and disc brakes are compared in Figure 15.

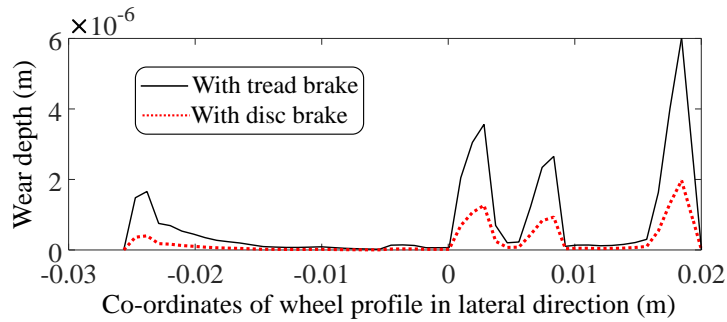


Figure 14. Wear distribution after 10,044 km travel with tread and disc brakes in front bogie front axle.

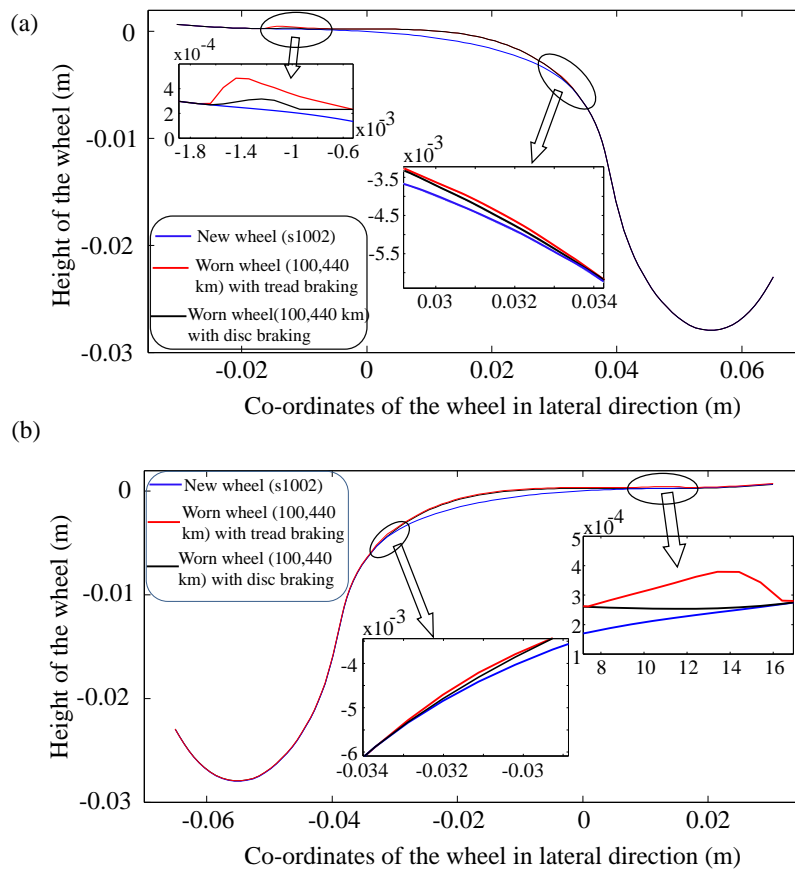


Figure 15. Worn wheel profiles with tread and disc braking after travelling 100,440 km distance: (a) left and (b) right wheel profiles of front axle of front bogie.

It is observed that tread braking causes more wear at the flange root and end of the tread of both the wheels (left and right) in comparison to disc braking. With tread braking, two simultaneous contact patches are intermittently observed in the worn wheel after 20,088 km distance covered by the vehicle. The secondary contact patch appears for a small duration in the initial stages and as the wheel wears out further, the duration of its appearance increases. In the worn wheel profile after 100,440 km, the secondary contact patch appears for a significantly longer time as shown in Figure 16 and the wear distribution changes. Further, the dynamic performance, such as creepage (longitudinal and lateral), creep forces (longitudinal, lateral and normal) of the worn wheel (after 100,440 km) has been studied (Figure 17; Figure 18). Note that the wear volume depends on the frictional power generated at the contacts. Power being a scalar quantity, the magnitudes of frictional

forces and slip velocities (creepages) can be used to compute it. Therefore, Figure 17; Figure 18 show the magnitudes of the creepages and creep forces. From the Figure 17; Figure 18, it is seen that the above-mentioned parameters (creepage and creep forces) are larger in the case of worn wheel (both primary and secondary contact patches) as compared to new wheel and hence there is more slip and wear. However, the normal contact force is less in worn wheel as compared to new wheel due to sharing of loads by the primary and secondary contact patches. Note that CP1 and CP2 indicate the primary and secondary contact patches, respectively. In a relatively new wheel-set, there is single contact patch which is denoted as CP. On the other hand, in older or worn-out wheel-set, both primary and secondary contact patches, CP1 and CP2, may exist at certain times whereas one contact patch CP1 can be present at certain other times. In such a situation, if CP2 location is shown as zero then it indicates absence of secondary contact patch. Correspondingly, the creepages and creep forces at secondary contact patch, when CP2 location is zero, are also zero.

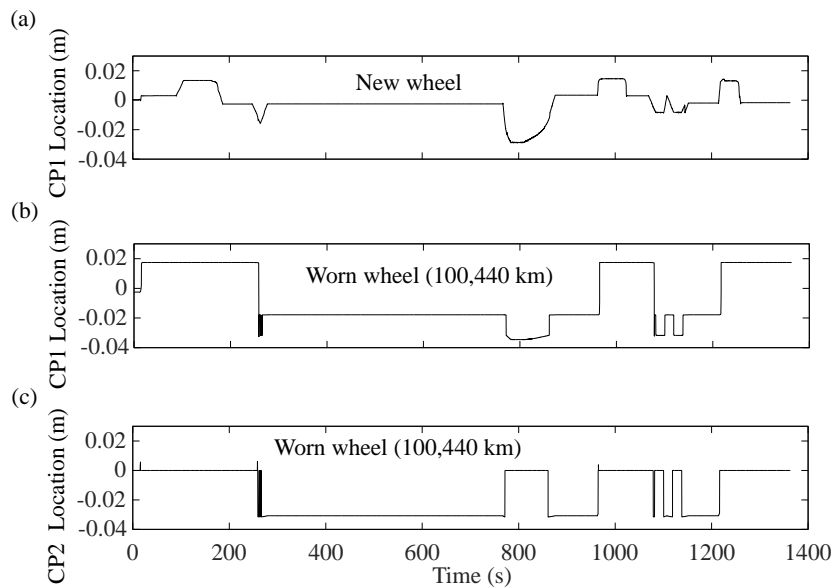


Figure 16. Location of the contact patch (CP) in (a) Lateral direction of the wheel during first 27.9 km distance travelled by the vehicle with new wheel, and (b) Locations of primary (CP1) and (c) secondary contact patches (CP2) for the worn wheel in the last 27.9 km distance travelled by the vehicle before reaching 100,400 km target.

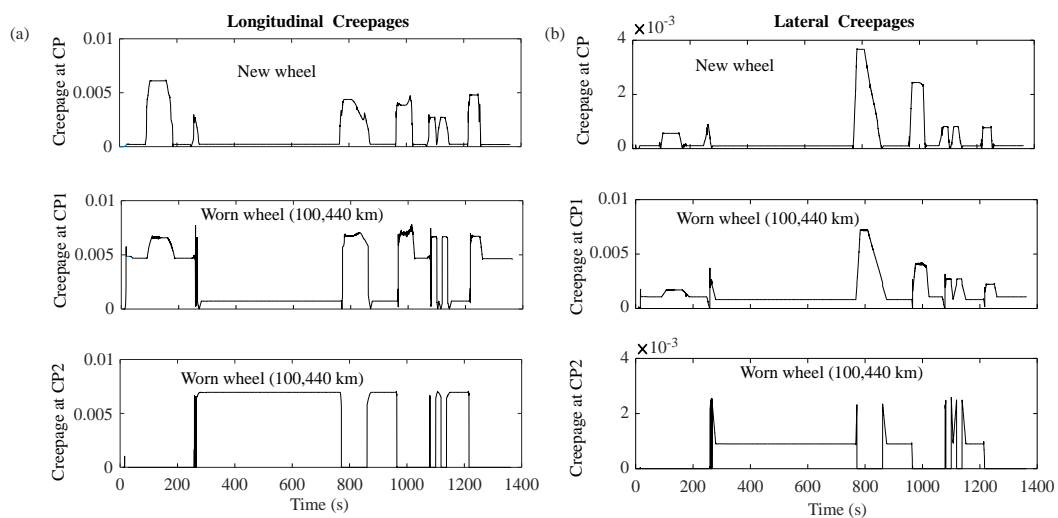


Figure 17. (a) Longitudinal and (b) lateral creepage magnitudes at contact patches (CP for new wheel, and CP1 and CP2 for worn wheel just before reaching 100,440 km target).

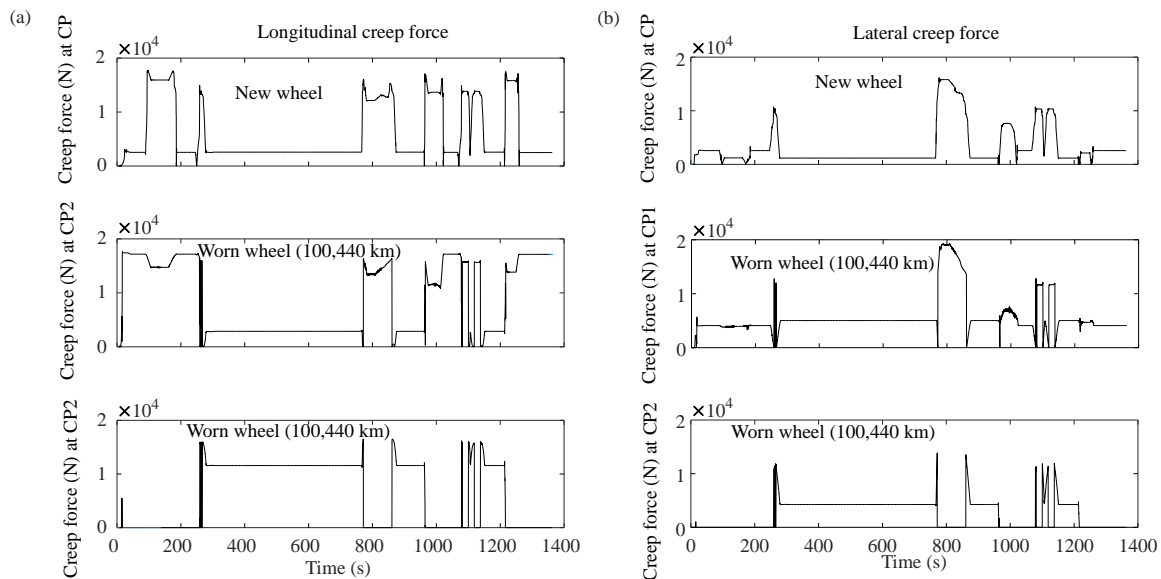


Figure 18. (a) Longitudinal and (b) lateral creep force magnitudes at contact patches (CP for new wheel, and CP1 and CP2 for worn wheel just before reaching 100,440 km target).

It can be seen that the longitudinal and lateral creep forces presented in Figure 18 follow the same trend as the corresponding creepages shown in Figure 17, but there is no proportional relation due to the use of Kalker's modified contact theory with non-linear creep force formulation [36,38]. Also, note that if CP2 location is zero in Figure 16, i.e., there is only one contact patch CP1 (CP2 does not exist), then the longitudinal and lateral creepages and creep forces at non-existent CP2 turnout to be zero in Figure 17; Figure 18.

5.1. Stability Assessment

Critical speed is the speed at which onset of vehicle hunting instability occurs. Actually, the vehicle operating speed is kept much below this threshold value. The curve negotiation and rate of recurrence of kinematic oscillation depend on the local conicities of wheel–rail pair and due to wear, the local conicities change. The phenomenon of the kinematic instability of the wheel-set in straight track can be found in Klingel's linear model [49,50]. It is necessary to focus on both the characteristics of wheel–rail coupling and the design parameters of the bogie to check the stability condition through dynamic simulations. Several approaches are used to determine critical speed of the vehicle [51]; out of which the initial lateral displacement (perturbation) of the wheel-set approach is used here. In this approach, the lateral displacement response of the wheel-set to the initial perturbation is determined on a straight/tangent track and the vehicle is considered to be stable if the amplitude of wheel set lateral oscillation reduces with time and becomes negligible as compared to flange-way clearance [52]. Small perturbation type (ramp with height and width 5 mm each) irregularities are given in the vertical direction of the track to excite the wheel-set to determine the critical speed. Note that vertical perturbation gives lateral perturbation due to conicity of the wheel.

Similarly, the derailment (wheel climb) speed is calculated in the same designed curved track by increasing the vehicle speed in discrete steps and simulating the vehicle dynamics over the entire track at a constant speed [53]. It is observed that the derailment occurs at the critical curved radius (maximum curvature zone in the track). The variation of critical and derailment speeds for different depths of wheel wear (in terms of distance covered by the vehicle) are shown in Figure 19. It is observed from the simulation results that the critical speed of new (unworn) wheel is 97 m/s (349 km/h), whereas the worn wheels up to 70,308 km distance covered by the vehicle gives slightly better critical speed and thereafter, the critical speed decreases rapidly. However, the derailment speed is almost constant as the wheel wear occurs at the flange root but not at the flange. Critical speed increases with decrease in the

tread gradient or conicity and decreases with increase in the conicity. Initially, the wheel tread wear reduces the wheel conicity at the nominal tread contact zone, i.e., makes the wheel more cylindrical at the tread center. As a consequence, the critical speed increases. Thereafter, with further wheel wear, the contact points on the wheel shift to tread end and flange root where the conicity is higher. Therefore, after a limiting amount of tread wear, the critical speed reduces sharply.

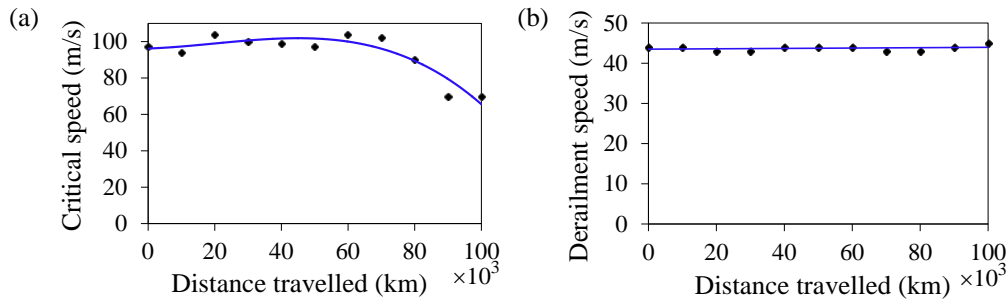


Figure 19. Variation of (a) critical speed and (b) derailment speed with distance travelled by the vehicle.

5.2. Derailment Quotient

Derailment quotient or Y/Q quotient [54] is defined as the ratio of lateral to vertical force which is used for the safety criteria. The vehicle is operated with the same velocity profile (as Figure 5) in the designed track. The absolute values of the Y/Q ratios of the left wheel of the front axle of the front bogie for new and worn wheels (100,440 km) are shown in Figure 20. The maximum value of the derailment quotient in a worn wheel and a new wheel is 0.435 and 0.2019, respectively. Thus, the derailment quotient in worn wheels is 53.6% higher than new wheels. The derailment quotient is a qualitative indicator of tendency to derail. This varies with the vehicle speed, curve radius, super elevation or cant, and other parameters. The vehicle reaches the steepest curve section of the track at about 800 s where the operating speed is reduced to about 16 m/s. The maximum value of the derailment quotient is observed in that section of the track. It is also seen that with the worn wheel, there is appreciable value of derailment quotient (approximately, 0.15) in the straight portion of the track. This happens due to repeated flange root contact, i.e., the contact points shifting away from the wheel tread center. The derailment quotient is obtained for the given operating speed which varies along the track. Note that in this research, the contact points stay between the tread-edge to the flange root. The derailment speed is the limiting speed at which the wheel jumps the rail, i.e., the flange climbs over the rail. Since the wear takes place at the tread and flange root, but not the flange face, the lateral force required for the wheel flange to climb over the rail remains almost unaffected (See Figure 19b). For more accurate estimation of derailment speed, which is compatible with the derailment quotient, the flange wear also needs to be accounted for in the wear model.

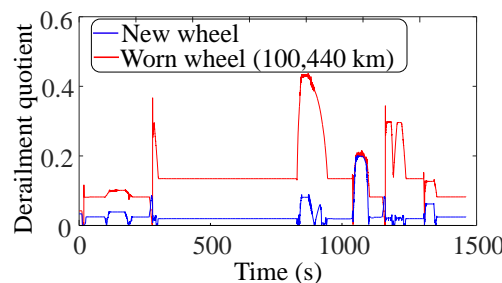


Figure 20. Derailment quotient for new and worn wheels (after 100,440 km) of left wheel of front axle of front bogie.

5.3. Wear Number

The wear rate can be indicated through the wear number [55–57], which is defined as the sum of creep force power of a wheel of the vehicle. As per Archard’s abrasive wear theory, the wear volume is assumed to be proportional to the frictional work. Therefore, wear number gives an assessment of rate of wear at different locations on vehicle along the track. The frictional power at a given location on the track varies with change in wheel profiles. For wear number calculation, the same predefined track (Figure 3) and velocity profile (Figure 5) are used. Since the wear during the braking is assumed to be predominantly in the brake pads which have lower modulus of elasticity in comparison to that of the wheel material (See the assumptions stated in Section 2), the frictional power generated at the brake pad–tread contact is omitted from wheels’ wear number computation. In the tread portion of the wheel, the frictional power due to spin creepage is usually neglected and the wear number is calculated as [54,58]

$$\text{Wear number} = \sum_{i=1}^{N_p} |f_x(i)v_x(i)| + |f_y(i)v_y(i)| \tag{19}$$

where $f_x(i)$ and $f_y(i)$ are the longitudinal and lateral creep forces, respectively, at the i^{th} contact patch and N_p is the number of contact patches. Note that the unit of wear number is N and it has to be multiplied with the vehicle forward velocity V to obtain the frictional power. The wear number, as per Equation (18), of the front left wheel of the front bogie for worn wheel and new wheel are shown in Figure 21 at various times or positions on the track. It is noted during simulation that the average wear number of worn wheel profile is increased by 80.35%. The wear number is large when the vehicle runs on a curve. Note that wear number gives a subjective assessment of wear rate whereas, in reality, the wear distribution on the lateral wheel profile is more significant in deciding the lifecycle of the wheels [54].

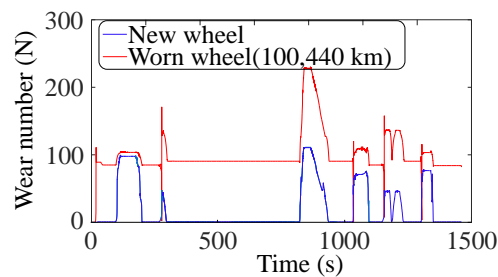


Figure 21. Wear number for new and worn wheels (after 100,440 km) of left wheel of front axle of front bogie.

5.4. Passenger Comfort

A qualitative indicator of passenger ride comfort is Sperling’s ride index (W_z) [59,60], which is given as

$$W_z = \left(\int_{f_1}^{f_2} a_f^2 B^2 df \right)^{1/6.67} \tag{20}$$

where f_1 and f_2 are lower and upper threshold frequencies, respectively, a_f is the amplitude of acceleration (obtained from fast Fourier transform) and B is the acceleration weighting factor. The frequency weighting factor in vertical and horizontal directions are, respectively, given as

$$\left. \begin{aligned} B_v &= 0.588 \left[\frac{1.911f^2 + (0.25f^2)^2}{(1 - 0.277f^2)^2 + (1.563f - 0.0368f^3)^2} \right]^{1/2} \\ B_l &= 1.25B_v \end{aligned} \right\} \tag{21}$$

In this paper, the ride comfort is evaluated both in straight and curved tracks (curve radius 2000 m and cant height 60 mm) with the measured type of irregularities, both in left and right sides of the track. The ride comfort is evaluated at the center of the car body. The vehicle runs at a speed of 22.5 m/s (81 kmph) and 16.8 m/s (60.48 kmph) in the straight and curved tracks, respectively. The variations of ride comfort at different depth of wear of the wheels (different in left and right) for both straight and curved tracks are shown in Figure 22, both in lateral and vertical directions. The distinct points indicate the ride indices which are evaluated after each 10,044 km distance travel and the solid line gives the trend. It is seen that the ride comfort is almost constant up to a certain depth of wear (100,440 km) both in lateral and vertical direction for both the tracks. Thereafter, there is increased flange contact due to which the ride comfort in the lateral direction reduces sharply, i.e., the Sperling ride index increases sharply. Sperling index value below 2.0 indicates a pleasant ride with noticeable vibrations whereas any value above 3.0 is classified as unpleasant. Note that the ride comfort also depends on the vehicle speed and track irregularity. The ride comfort reduces when the track is more irregular or the vehicle speed is higher, which amplifies the base excitations to the vehicle. At certain track excitation frequencies, ride comfort may reduce due to resonance effects. Also, the duration of travel can alter the ride comfort. Therefore, ISO 2631 analysis, as given in [61], may be used for better evaluation of ride comfort.

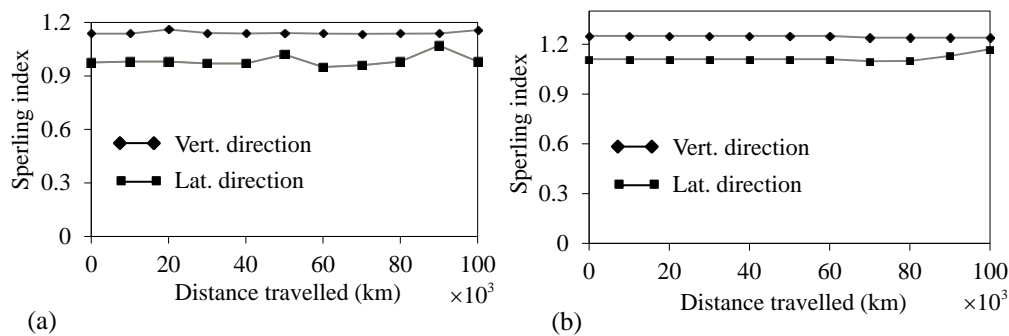


Figure 22. Sperling's ride comfort (W_z) in (a) straight track and (b) curved track with measured (stochastic) type irregularities.

6. Discussion

This paper presents a computational tool to predict wear due to tread braking in the railway vehicle in more realistic and generalized working conditions. This wear prediction tool is more robust as thermo-mechanical effect has been considered on the wheel due to braking. This model consists of three mutually interactive parts: (i) the multi-body vehicle model which gives global wheel-rail contact parameters such as creep force and creepage, etc. to calculate brake power at the wheel-rail and wheel-block interfaces, (ii) the thermal model which gives the temperature distribution in wheel tread during the length of travel and (iii) the wear evolution model where the change in material properties due to elevated temperature is imported for wear calculation. Again, the wear evolution model consists of contact model and wear model. The Hertzian and modified FASTSIM approaches are used to calculate normal and tangential pressure, respectively. Three-dimensional transient FE analysis has been done to model frictional heating due to tread braking and heat conduction through the contact patch at the rail and wheel interface. The maximum wheel temperature has been estimated with time for different rates of deceleration and stop braking. The maximum wheel temperature is reached to 665.7 °C at the wheel-tread during the stop braking. Due to elevated temperature, changes in material properties such as elastic modulus, density and Poisson's ratio have been taken into consideration during wear calculation. After covering each 10,044 km distance the wheel profile is updated and total distance covered by the vehicle is 100,440 km. The dynamic performance, such as critical and derailment speed, wear index and derailment quotient of the vehicle has been studied for different depth of wear.

The approach implemented here can predict the average life span and re-profiling schedule of the wheel, based on the dynamic performance, such as critical speed and derailment quotient. It is recommended that re-profiling may be necessary after 100,440 km as the creep forces and creepage are much more as compared to new wheel which leads to increase the wear rate abruptly. This distance corresponds to an almost one-year operation with daily five times up and down shuttle journeys between the two considered stations. This one-year wheel re-profiling/maintenance schedule well-correlates with the maintenance practice followed by the Indian railways in the track sectors with too many curves.

However, the plastic deformation of the wheel affects the wear distribution as the microstructure of the wheel material changes at a high temperature. This influence may be considered as future research. The track switches and weather conditions may be included to enhance the accuracy of the model. It is also observed from multi-body dynamics simulation that temporary secondary contact patches at flange/flange root appear during simulations in the case of worn wheels on entry and exit from the curves. It has been hypothesized that very small duration contact at small sized secondary contact patches (with small normal force) do not cause significant wear at the flange/flange root. In this study, wear distribution is estimated due to single point contact patch which may be extended for multiple contact patches to verify the afore-mentioned postulation. Moreover, according to flash temperature theory and experimental evidence [25], phase transformation occurs above the austenitization temperature of approximately 700 °C [62], whereas the maximum temperature observed in the current study is below that limit (See Figure 10). If the vehicle speed and the brake power are increased further, then phase transformation can also be factor in thermal and wear models. Above flash temperature, wheel shelling becomes predominant and other modes of wear need to be accounted for in the model.

Although the rail wear is neglected in this study, it can be computed by using a similar procedure presented here for the wheel wear and the same procedure in various forms has been adopted by many researchers [58,63]. ADAMS VI-Rail [64–67] allows defining variable rail cross-section for turn-outs and the same can be used to define a track with variable levels of rail wear. The rail wear evolution model follows the same process of dynamic simulation, contact patch discretization, wear depth computation and rail profile updating [26,40,44]. The rail wear occurs mostly in the rail top and inner face and it depends on several factors such as the number of axle passes, the corresponding vehicles' tonnage and speed, curve radius and other track geometry parameters.

Both rail profile and wheel profile influence the vehicle dynamics. Therefore, wheel wear influences rail wear and vice versa. The rail top wear and wheel tread wear combine to change the equivalent conicity on straight tracks and hence influence the critical speed of the vehicle. Whereas, the flange wear and rail inner face wear combine to affect the derailment speed. As the rail top and wheel tread become flatter, hunting oscillations and multipoint or conformal contact become commonplace. Also, the curving performance of the vehicle deteriorates, and the wheels tend to shift by a large amount in order to negotiate a curve; thereby causing repeated impact of the worn flange with the worn inner face of the rail. This increases the rate of flange, flange root, inner rail face and rail corner wear. In fact, a vehicle with worn wheel contributes to increased rate of rail wear and a track with worn rails contributes to increased rate of wheel wear. With worn track and wheels, the critical speed reduces significantly and the passenger comfort is also reduced due to repeated flanging in the curves (Sperling ride index [60] in the lateral direction increases severely).

In this article, the wheel wear is distributed over the entire tread region with rotational symmetry. Under wheel locking/burn-out, there can be severe localized wear leading to wheel flat. However, further wear evolution after the wheel flat, material property changes, its influence on vehicle hunting stability and derailment etc. may be addressed by following the approach presented in this article. Wheel wear can be reduced significantly by using radially steered bogies as reported in [60]. Active radial steering of bogies is performed through automation and it requires the vehicle speed, load, and the local parameters of the track (cant or super-elevation, radius of curvature, etc.) as input to the

steering controller. Vehicle speed and load are obtained from onboard sensors whereas local track parameters are obtained from a lookup table after localizing the vehicle either through sensing the track side markers from the vehicle or through wireless transmission from way-side stations. Global positioning systems are also being used for vehicle localization [68] in order to regulate speed and steering. Such speed and steering regulations reduce the wheel and rail wear, and chance of derailment; thereby increasing the life of the rail and the rolling stock, and passenger safety. The study presented in [60] does not consider the influences of braking in the steering bogies and can be improvised further in the lines proposed here.

Author Contributions: Conceptualization and methodology, A.K.S.; software, validation, formal analysis and investigation, S.P.; writing—original draft preparation, S.P.; writing—review and editing, A.K.S.; supervision, A.K.S.

Acknowledgments: The authors thank Prof. Vikranth Racherla, Center for Railway Research, IIT Kharagpur, for his constructive comments and suggestions. The authors thank Prof. Shiv Brat Singh, Department of Metallurgical & Materials Engineering, IIT Kharagpur, for providing the material properties (Figure 12) and valuable suggestions.

Conflicts of Interest: The authors declare no conflict of interest.

Nomenclature

a and b	Semi-major and semi-minor axes of the contact patch, respectively (mm).
A_0	Ratio of friction coefficient (μ_∞ / μ_0)
B_0	Coefficient of exponential friction decrease (s/m)
c_{ij}	Kalker's parameters
C_p	Specific heat capacity of the material (J/kg °C)
f	Traction force at contact patch (N) /frequency of vibration
F_b	Braking force (N).
f_x and f_y	Longitudinal and lateral creep forces, respectively (N)
E and G	Young's modulus and Shear modulus (GPa).
H_b	Brake block width (m)
h_{wr}	Thermal conductance (W/m ² °C)
I_w	Wear index (N/mm ²)
J	Polar moment of inertia of wheel and axle (N/m ²)
\mathbf{K}	Thermal conductivity matrix
L	Flexibility function
L_b	Brake block length (m)
n_w^r	Unit vector normal to the wheel surface
N	Normal contact force (N)
N_p	Total number of contact patches
n_x and n_y	Numbers of cells in the contact patch in x and y directions, respectively.
\mathbf{P}_A and \mathbf{P}_t	Adhesion limit pressure (N/m ²) and tangential pressure (N/m ²)
P_0	Maximum pressure in the pressure distribution (N/m ²)
q_{brake}	Mean heat flux over the brake block contact area (J/m ² s)
Q_{conv}	Amount of heat transfer through the convection (J/s)
R	Mean radius of the wheel at nominal tread region (m)
R_x and R_y	Reactions at axle in the x and y directions, respectively (N)
s	Total slip (m/s)
t	Time duration (s)
\mathbf{v}	Velocity vector of spatial points (m/s)
T and T_r	Instantaneous temperature (°C) and ambient temperature (°C)
\mathbf{u}	Elastic displacement (m)
V	Peripheral velocity of the wheel (m/s)
w	Rigid slip (m/s)
w_n and w_o	New and old wheel profiles
Y and Q	Lateral and vertical forces, respectively (N)

α	Heat transfer coefficient (W/Km ² or W/°Cm ²)
ξ	Global creepage vector
β	Heat partition factor
Δ	Thermal penetration depth (m)
δ_p	Specific volume of removed material
κ	Thermal diffusivity (m ² /s)
λ	Thermal conductivity (W/m °C)
ρ	Mass density (kg/m ³)
ω	Angular velocity of the wheel (rad/s)
∇	Vector differential operator
μ and μ_k	Coefficients of static and kinematic friction
μ_0 and μ_∞	Maximum friction coefficient at zero slip and at infinity slip velocity
v_x, v_y, ϕ	Longitudinal and lateral creepages (dimension-less), and spin creepage (m ⁻¹)
ν	Poisson's ratio

References

1. Laraqi, N. Velocity and relative contact size effects on the thermal constriction resistance in sliding solids. *ASME J. Heat Transf.* **1997**, *119*, 173–177. [[CrossRef](#)]
2. Vernersson, T. Thermally induced roughness of tread braked railway wheels, Part 1: Brake rig experiments. *Wear* **1999**, *236*, 96–105. [[CrossRef](#)]
3. Vernersson, T. Thermally induced roughness of tread braked railway wheels, Part 2: Modeling and field measurements. *Wear* **1999**, *236*, 106–116. [[CrossRef](#)]
4. Godet, M. The third-body approach: A mechanical view of wear. *Wear* **1984**, *100*, 437–452. [[CrossRef](#)]
5. Tanvir, M.A. Temperature rise due to slip between wheel and rail—an analytical solution for Hertzian contact. *Wear* **1980**, *61*, 295–308. [[CrossRef](#)]
6. Knothe, K.; Liebelt, S. Determination of temperatures for sliding contact with applications for wheel-rail systems. *Wear* **1995**, *189*, 91–99. [[CrossRef](#)]
7. Ertz, M.; Knothe, K. A comparison of analytical and numerical methods for the calculation of temperatures in wheel/rail contact. *Wear* **2002**, *253*, 498–508. [[CrossRef](#)]
8. Ma, Y.; Markine, V.; Mashal, A.A.; Ren, M. Modelling verification and influence of operational patterns on tribological behaviour of wheel-rail interaction. *Tribol. Int.* **2017**, *114*, 264–281. [[CrossRef](#)]
9. Tudor, A.; Radulescu, C.; Petre, I. Thermal effect of the brake shoes friction on the wheel/rail contact. *Tribol. Ind.* **2003**, *25*, 27–32.
10. Spiriyagin, M.; Lee, K.S.; Yoo, H.H.; Kashura, O.; Popov, S. Numerical calculation of temperature in the wheel–rail flange contact and implications for lubricant choice. *Wear* **2010**, *268*, 287–293. [[CrossRef](#)]
11. Naeimi, M.; Li, S.; Li, Z.; Wu, J.; Petrov, R.H.; Sietsma, J.; Dollevoet, R. Thermomechanical analysis of the wheel-rail contact using a coupled modelling procedure. *Tribol. Int.* **2018**, *117*, 250–260. [[CrossRef](#)]
12. Chen, W.W.; Wang, Q.J. Thermomechanical analysis of elastoplastic bodies in a sliding spherical contact and the effects of sliding speed, heat partition and thermal softening. *J. Tribol.* **2008**, *130*, 041402. [[CrossRef](#)]
13. Kennedy, T.C.; Plengsaard, C.; Harder, R.F. Transient heat partition factor for a sliding railcar wheel. *Wear* **2006**, *261*, 932–936. [[CrossRef](#)]
14. Teimourimanesh, S.; Vernersson, T.; Lunden, R. Thermal capacity of tread-braked railway wheels. Part 1: Modelling. *J. Rail Rapid Transit* **2016**, *230*, 784–797. [[CrossRef](#)]
15. Teimourimanesh, S.; Vernersson, T.; Lunden, R. Thermal capacity of tread-braked railway wheels. Part 2: Application. *J. Rail Rapid Transit* **2016**, *230*, 798–812. [[CrossRef](#)]
16. Ahlström, J.; Kabo, E.; Ekberg, A. Temperature-dependent evolution of cyclic stress of railway wheel steel. *Wear* **2016**, *366*, 378–382. [[CrossRef](#)]
17. Cole, K.D.; Tarawneh, C.M.; Fuentes, A.A.; Wilson, B.M.; Navarro, L. Thermal models of railroad wheels and bearings. *Int. J. Heat Mass Transf.* **2010**, *53*, 1636–1645. [[CrossRef](#)]
18. Peters, J.C.; Eifler, D. Influence of service temperatures on the fatigue behavior of railway wheel and tyre steels. *Mater. Test.* **2009**, *51*, 748–754. [[CrossRef](#)]
19. Ahlström, J.; Karlsson, B. Microstructure evaluation and interpretation of the mechanically and thermally affected zone under railway wheel flat. *Wear* **1999**, *232*, 1–14. [[CrossRef](#)]

20. Ahlström, J.; Karlsson, B. Analytical 1D model for analysis of the thermally affected zone formed during railway wheel skid. *Wear* **1999**, *232*, 15–24. [[CrossRef](#)]
21. Asih, A.M.S.; Ding, K.; Kapoor, A. Modelling the effect of steady state wheel temperature on rail wear. *Tribol. Lett.* **2013**, *49*, 239–249. [[CrossRef](#)]
22. Walia, M.S. Towards Enhanced Mechanical Braking Systems for Trains. Ph.D. Thesis, Chalmers University of Technology, Gothenburg, Sweden, 2017.
23. Yang, Z.; Li, Z.; Dollevoet, R. Modelling of non-steady-state transition from single-point to two-point rolling contact. *Tribol. Int.* **2016**, *101*, 152–163. [[CrossRef](#)]
24. Galas, R.; Kvarda, D.; Omasta, M.; Krupka, I.; Hartl, M. The role of constituents contained in water-based friction modifiers for top-of-rail application. *Tribol. Int.* **2018**, *117*, 87–97. [[CrossRef](#)]
25. Archard, F. The temperature of rubbing surfaces. *Wear* **1959**, *2*, 438–455. [[CrossRef](#)]
26. Pradhan, S.; Samantaray, A.K.; Bhattacharyya, R. Prediction of railway wheel wear and its influence on the vehicle dynamics in a specific operating sector of Indian railways network. *Wear* **2018**, *406–407*, 92–104. [[CrossRef](#)]
27. Enblom, R.; Berg, M. Simulation of railway wheel profile development due to wear: Influence of disk braking and contact environment. *Wear* **2005**, *258*, 1055–1063. [[CrossRef](#)]
28. Newcomb, T.P. Thermal aspects of railway braking. In Proceedings of the IMechE International Conference on Railway Braking, University of York, York, UK, 26–27 September 1979; pp. 7–18.
29. Balakin, V.A.; Sergienko, V.P.; Komkov, O.Y. Heat transfer in friction contact zone at engagement of disc clutches and brakes. *Sov. J. Frict. Wear* **1997**, *18*, 450–455.
30. Tian, X.; Kennedy, F.E., Jr. Maximum and average flash temperatures in sliding contacts. *ASME J. Tribol.* **1994**, *116*, 167–174. [[CrossRef](#)]
31. Teimourimanesh, S.; Vernersson, T.; Lundén, R. Modeling of temperatures during railway tread braking: Influence of contact conditions and rail cooling effect. *J. Rail Rapid Transit* **2014**, *228*, 93–109. [[CrossRef](#)]
32. Rafei, M.; Ghoreishy, M.H.R.; Naderi, G. Thermo-mechanical coupled finite element simulation of tire cornering characteristics—Effect of complex material models and friction law. *Math. Comput. Simul.* **2018**, *144*, 35–51. [[CrossRef](#)]
33. Kragelski, I.V.; Dobycyn, M.N.; Kombatov, V.S. *Friction and Wear: Calculation Methods*; Pergamon Press: Oxford, UK, 1982.
34. Polach, O. Creep forces in simulations traction vehicles running on adhesion limit. *Wear* **2005**, *258*, 992–1000. [[CrossRef](#)]
35. Dufrenoy, P. Etude du comportement thermomecanique des disques de freins vis a vis risques de defaillance ((Study of thermomechanical behavior of brake discs vis-à-vis risk of failure). Ph.D. Thesis, Universite des Science et Technologies de Lille, Cité Scientifique, France, 1995.
36. Fischer, F.D.; Werner, E.; Knothe, K. The surface temperature of a half plane heated by friction and cooled by convection. *Z. Angew. Math. Mech.* **2001**, *81*, 75–81. [[CrossRef](#)]
37. Baehr, H.D.; Stephan, K. *Heat and Mass Transfer*; Springer: Berlin, Germany, 1998.
38. Kalker, J.J. *Three-dimensional Elastic Bodies in Rolling Contact*; Kluwer Academic Publishers: Dordrecht, The Netherlands, 1990.
39. Dukkipati, R.V.; Amyot, J.R. *Computer Aided Simulation in Railway Dynamics*; Marcel Dekker: New York, NY, USA, 1988.
40. Auciello, J.; Ignesti, M.; Malvezzi, M.; Meli, E.; Rindi, A. Development and validation of a wear model for the analysis of the wheel profile evolution in railway vehicles. *Veh. Syst. Dyn.* **2012**, *50*, 1707–1734. [[CrossRef](#)]
41. Saunders, N.; Guo, U.K.Z.; Li, X.; Miodownik, A.P.; Schillé, J.P. Using JMatPro to model materials properties and behavior. *J. Miner. Metals Mater. Soc. JOM* **2003**, *55*, 60–65. [[CrossRef](#)]
42. Pombo, J.; Ambrosio, J.; Pereira, M.; Lewis, R.; Dwyer-Joyce, R.; Ariaudo, C.; Kuka, N. Development of a wear prediction tool for steel railway wheels using three alternative wear functions. *Wear* **2011**, *271*, 238–245. [[CrossRef](#)]
43. Braghin, F.; Lewis, R.; Dwyer-Joyce, R.S.; Bruni, S. A mathematical model to predict railway wheel profile evolution due to wear. *Wear* **2006**, *261*, 1253–1264. [[CrossRef](#)]
44. Ignesti, M.; Marini, L.; Meli, E.; Rindi, A. Development of a model for the prediction of wheel and rail wear in the railway field. *J. Comput. Nonlinear Dyn.* **2012**, *7*, 041004. [[CrossRef](#)]

45. Zhu, Y.; Olofsson, U.; Nilson, R. A field test study of leaf contamination on railhead surfaces. *J. Rail Rapid Transit* **2014**, *228*, 71–84. [[CrossRef](#)]
46. Olofsson, U.; Zhu, Y.; Abbasi, S.; Lewis, R.; Lewis, S. Tribology of the wheel–rail contact—aspects of wear, particle emission and adhesion. *Veh. Syst. Dyn.* **2013**, *51*, 1091–1120. [[CrossRef](#)]
47. Nikas, G.K. A mechanistic model of spherical particle entrapment in elliptical contacts. *Proc. Ins. Mech. Eng. Part J J. Eng. Tribol.* **2006**, *220*, 507–522. [[CrossRef](#)]
48. Frischmuth, K.; Langemann, D. Numerical calculation of wear in mechanical systems. *Math. Comput. Simul.* **2011**, *81*, 2688–2701. [[CrossRef](#)]
49. Esveld, C. *Modern Railway Track*, 2nd ed.; MRT-Productions: Delft, The Netherlands, 2001.
50. Iwnicki, S. *The Manchester Benchmarks for Rail Vehicle Simulators*; Swets and Zeitlinger: Lisse, The Netherlands, 1999.
51. Banerjee, N.; Karmakar, R. Modelling of a free rail wheel-set using non-linear creep force. *Int. J. Heavy Veh. Syst.* **2014**, *21*, 310–327. [[CrossRef](#)]
52. Banerjee, N.; Karmakar, R. Bond graph modeling of rail wheel-set on curved track. *Simulation* **2007**, *83*, 695–706. [[CrossRef](#)]
53. Banerjee, N.; Saha, A.K.; Karmakar, R.; Bhattacharyya, R. Bond graph modeling of a railway truck on curved track. *Simul. Model. Pract. Theory* **2009**, *17*, 22–34. [[CrossRef](#)]
54. Polach, O.; Berg, M.; Iwnicki, S. Simulation. In *Handbook of Railway Vehicle Dynamics*; Iwnicki, S., Ed.; CRC Press: Boca Raton, FL, USA, 2006; pp. 359–421.
55. Orlova, A.; Boronenko, Y. The anatomy of railway vehicle running gear. In *Handbook of Railway Vehicle Dynamics*; Iwnicki, S., Ed.; CRC Press: Boca Raton, FL, USA, 2006; pp. 39–83.
56. Berthe, D.; Dowson, D.; Godet, M.; Taylor, C.M. (Eds.) *Tribological Design of Machine Elements*; Elsevier: Amsterdam, The Netherlands, 1989.
57. Santamaría, J.; Vadillo, E.G.; Oyarzabal, O. Wheel–rail wear index prediction considering multiple contact patches. *Wear* **2009**, *267*, 1100–1104. [[CrossRef](#)]
58. Hwang, I.K.; Hur, H.M.; Kim, M.J.; Park, T.W. Analysis of the active control of steering bogies for the dynamic characteristics on real track conditions. *Proc. Ins. Mech. Eng. Part F J. Rail Rapid Transit* **2018**, *232*, 722–733. [[CrossRef](#)]
59. Garg, V.K.; Dukkipati, R.V. *Dynamics of Railway Vehicle Systems*; Academic Press: Cambridge, MA, USA, 1984.
60. Samantaray, A.K.; Pradhan, S. Dynamic Analysis of Steering Bogies. In *Handbook of Research on Emerging Innovations in Rail Transportation Engineering*; Umesh Rai, B., Ed.; IGI Global: Hershey, PA, USA, 2016; pp. 524–579.
61. Pradhan, S.; Samantaray, A.K. Integrated modeling and simulation of vehicle and human multi-body dynamics for comfort assessment in railway vehicles. *J. Mech. Sci. Technol.* **2018**, *32*, 109–119. [[CrossRef](#)]
62. Nikas, G.K. Modeling dark and white layer formation on elasto-hydrodynamically lubricated steel surfaces by thermomechanical indentation or abrasion by metallic particles. *J. Tribol.* **2015**, *137*, 031504. [[CrossRef](#)]
63. Li, X.; Yang, T.; Zhang, J.; Cao, Y.; Wen, Z.; Jin, X. Rail wear on the curve of a heavy haul line—Numerical simulations and comparison with field measurements. *Wear* **2016**, *366*, 131–138. [[CrossRef](#)]
64. Ward, A.; Lewis, R.; Dwyer-Joyce, R.S. Incorporating a railway wheel wear model into multi-body simulations of wheelset dynamics. *Tribol. Ser.* **2003**, *41*, 367–376.
65. Lewis, R.; Braghin, F.; Ward, A.; Bruni, S.; Dwyer-Joyce, R.S.; Bel Knani, K.; Bologna, P. Integrating Dynamics and Wear Modelling to Predict Railway Wheel Profile Evolution. In *6th International Conference on Contact Mechanics and Wear of Rail/Wheel Systems*; Ekberg, A., Kabo, E., Ringsberg, J., Eds.; CHARMEC: Gothenburg, Sweden, 2003; pp. 7–16.
66. Shevtsov, I.Y.; Markine, V.L.; Esveld, C. Optimal design of wheel profile for railway vehicles. *Wear* **2005**, *258*, 1022–1030. [[CrossRef](#)]

67. Jahed, H.; Farshi, B.; Eshraghi, M.A.; Nasr, A. A numerical optimization technique for design of wheel profiles. *Wear* **2008**, *264*, 1–10. [[CrossRef](#)]
68. Jo, H.J.; Kwak, S.W.; Yang, J.M. Vehicle Localization Using Internal Sensors and Low-Cost GPS for Autonomous Driving. *J. Korean Inst. Intell. Syst.* **2017**, *27*, 209–214. [[CrossRef](#)]



© 2019 by the authors. Licensee MDPI, Basel, Switzerland. This article is an open access article distributed under the terms and conditions of the Creative Commons Attribution (CC BY) license (<http://creativecommons.org/licenses/by/4.0/>).